UNIVERSITÁ DEGLI STUDI DI PADOVA

Dipartimento di Ingegneria Industriale DII

Laurea Magistrale in Ingegneria dell'Energia Elettrica

Design of a current oversampling board for electrical drives

Experimental testing in a machine parameters evaluation

Progetto di una scheda per il sovracampionamento della corrente di un azionamento elettrico

Sperimentazione nella valutazione dei parametri di macchina

Relatore: Ch.mo prof. Bolognani Silverio

Correlatore: Dr. Ing. Luca Peretti, ABB Corporate Research - Västerås - SE

Laureando: Michielin Diego 1132373

Anno Accademico 2017/2018

This project deals with the design of an electronic apparatus capable of high-speed oversampling (in the order of MHz) of the stator currents in an electric machine. The project includes the experimental evaluation of the design for a subsequent real-time estimation of machine parameters. The following list specifies the main parts of the project:

- Review of the current sensing technologies capable of oversampling.
- Current PCB design upgrade for oversampling capabilities.
- Prototype realization and mounting into the laboratory setup.
- Experimental validation through the measurement of current ripple.

The thesis was performed at the ABB Corporate Research in Västerås, Sweden, from September 25, 2017 to March 23, 2018.

Contents

List of abbreviations

AMR	Anisotropic magneto resistive
$CMRR$	Common Mode Voltage Rejection
CS	Current sensor
EMF	Electromotive force
EMI	Electromagnetic interference
FFt	Fast Fourier Transform
$FPGA$	Field-programmable gate array
FSF	Frequency scale factor
IIR	Infinite Impulse Response
IM	Induction motor
IPM	Interior Permanent Magnet motor
I/O	Input/output
$op-amp$	Operational amplifier
PCB	Printed circuit board
$PMASynRM$	Permanent Magnet Assisted Synchronous Reluctance Motor
PWM	Pulse width modulation
RMS	Root mean square
$SynRM$	Synchronous reluctance motor
tf	Transfer function

Introduction

Motivation

The good performances achieved by modern variable speed electric drives is obtain at expenses of more stress and degradation of the machine. Due to this fact, the analysis of stress phenomena is an active research area.

The steep voltage edges induced by the PWM output of the inverter produce surges at the machine terminal. The insulation of the machine suffers under these transient overvoltages. Studies showed that it is possible to assess the degradation on stator insulators by analyzing the magnitude of the initial peak appearing in the phase current at the switching instants: indeed the high frequency content of this response is related to the parasitic capacitances model of the machine, and thus informations about the quality of the stator insulation can be gleaned [1]. In particular the ringing phenomena in the early stage, visible in the figure 1, is due to the stray capacitances that change as a function of the ageing of insulators [2].

The overshoot typically consists of high frequencies in the range of (4-6 MHz) (see figure 2). The measuring system must have high bandwidth and fast sampling in-order to capture interesting transients - at least double of the maximum expected frequency, according to the Nyquist theorem. This high resolution can be used for verify the aging model.

More-over, a large current harmonic content could be used to build more accurate sensor-less drives by using an intrinsic high-frequency injection due to the PWM. The idea, proposed in several papers [3] and [4], concerns the exploitation of the PWM harmonics - developed by the stator currents - in order to assess the electrical rotor position estimation. The oversampling of motor currents allows furthermore a low-noise calculation of the current derivative (di/dt), which improves the measurement resolution and allows smooth operation down to zero speed without negative side-effects, such as acoustic noise [5]. This concept requires best performance characteristics for phase current sensing in terms of dynamic range and bandwidth. An upgraded hardware is thus necessary.

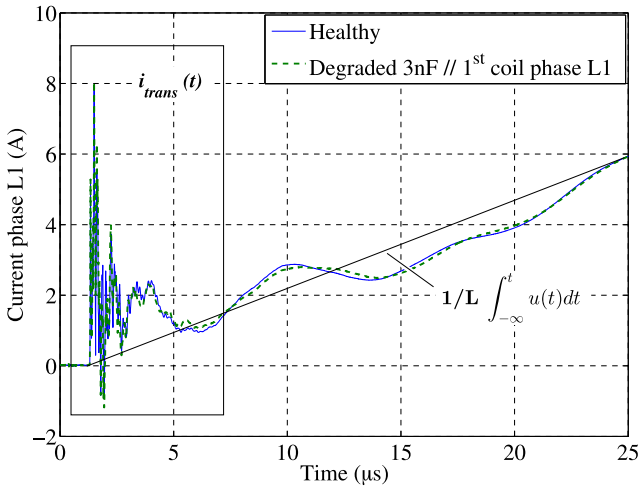

Figure 1: Current response after step excitation, comparison between healthy state machine and degraded insulation [2].

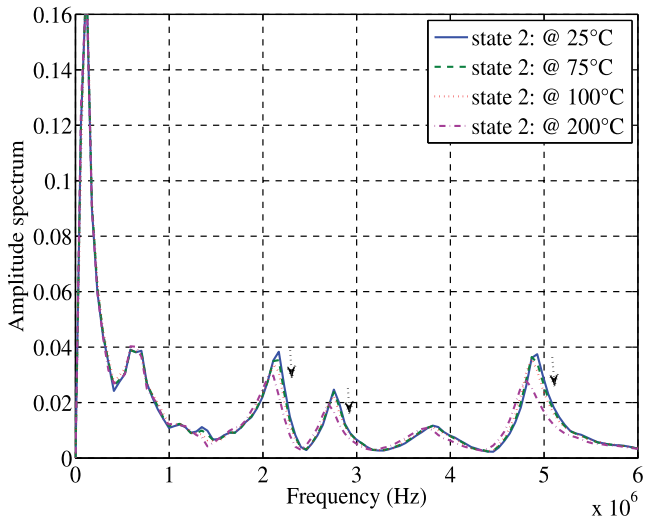

Figure 2: FFt of the sampled current, comparison between different temperatures [2].

Scope

The work aims at building an upgraded measuring printed circuit board for the phase current oversampling. Although both these problems have been already studied in several papers (up to this point), hardware limitations occur through poor dynamic features of the measuring system [6] [7].

The first stage of the work focuses on the choice of the best current sensor - in terms of bandwidth the target set at 5 MHz - available on the market. Different current sensing techniques are compared, taking into account the system requirements. The Sensitec CMS3050 is chosen, whose declared frequency bandwidth is 2 MHz (when on-board RC filtering is applied). Later on, the chosen device is tested in order to know its dynamic behavior without RC filter. Analog filters are designed to reach the targeted time response at the instant of switching.

Starting from the previous measurement box the PCB design is upgraded with the advanced requirements: the current sensors and the analog filters are embedded, a new geometry is chosen and a new type of connectors is mounted. The board is tested in the lab and at the end some remarks on the work and on future applications are done.

Structure

This report has the following structure.

The Introduction (this section) describes the motivation and scope of this document.

The Chapter 1 presents the review of current sensing technologies for high-speed oversampling. The main requirements taken into account are discussed for each considered technique.

The Chapter 2 describes in details the chosen current sensor, Sensitec CMS3050. The physical aspects are explained and the electrical data are summarized.

The Chapter 3 analyses frequency response and conditioning of the new device output.

The Chapter 4 describes the upgraded design of the printed circuit board. The PCB design is done with KiCad and new requirements are embedded in the board.

The Chapter 5 describes the tests carried out on the PCB: good results is reached although some further investigations are required.

The Conclusions reports conclusive remarks on the work.

The Future works indicates how the results of this report will be used in future activities.

The References specifies some material for further reading.

Chapter 1

Current sensing techniques

The project starts by searching a current sensor with a bandwidth suitable for the oversampling task. Therefore, this first chapter provides an overview of state-of-art current sensing techniques, taking into account system requirements. The following chapter instead will concern the choice and the explanation of the magneto-resistive sensor "Sensitec CMS3050".

1.1 Introduction

Current sensing is required in a wide range of electrical and electronics applications. The measurement of current ranges from µA to tens of thousands Amperes. It is self-evident that each technology has different performance in terms of cost, sensitivity, precision, bandwidth, measurement range and size. These features are factors that should be weighted along with the specific requirements of the application in making the selection. More-over, the current information needs to be available in a digital form for control or monitoring purposes and this means that output signal has to be acquired by an analog-to-digital converter.
Nowadays the research in the current technology area is focusing on devices with a range of several hundreds of amps, compact dimensions and high bandwidth. The requirements for this last parameter is rising into the MHz range in order to increase the power density and to sense high-speed current arising from static converters [5].
A common way to classify the current sensors is based upon the underlying physical principle:

- Magnetic field sensors
- Faraday's law of induction
- Ohm's law

The general requirements are instead:

- High sensitivity and high accuracy
- High bandwidth
- DC and AC measurements
- Low power consumption

- Reasonable price
- EMI rejection

In this project, only the techniques suitable for the purpose have been considered. The system (see figure Figure 1.1) is installed in the Motors and drives laboratory, located in ABB Corporate Research Västerås, Sweden. The application concerns the field of motor control. In particular, the set up consists of a motor (SynRM, PMASynRM, IM, IPM) fed by a three-phase inverter; the voltage in the DC-bus of the static converter is 560 V while the nominal RMS value of the current is around 50 A.

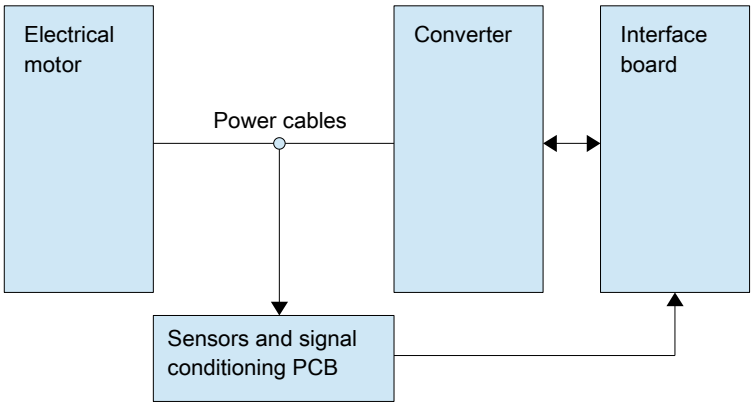

Figure 1.1: Inverter-fed motor with the current sensors.

The technologies taken into account from an oversampling perspective are:

- Hall-effect sensor
- Rogowski coil
- HOKA principle
- Current Viewing Resistor
- Magneto-resistive sensor

1.2 Hall-effect based sensor

This device, present in the previous measurement box [**?**], senses the primary current flowing through it thanks to the variation of a magnetic field. It is a common device in the current sensing technology.
The Hall effect was discovered in 1879 and states that if a current B flows through a conductive material permeated by a magnetic flux density B, a voltage v appears on the two faces of the material, in a direction perpendicular to both current and field. The equation states

$$v = \frac{IB}{nqd} \tag{1.1}$$

where n is the charge density, q is the charge carrier and d the thickness of the material where current flows.

The physical principle behind this effect is the renowned Lorentz force, stated below in a vectorial form:

$$\overline{F} = q \cdot (\overline{B} \times \overline{v}) \tag{1.2}$$

In fact the electrical current consists in the motion of charge carriers (electrons, holes or ions) which, in the presence of a magnetic field, experience the above-mentioned force and curve their paths, accumulating in one layer of the conductive material. Therefore, on the two faces a voltage gradient - called Hall voltage and proportional to the magnetic field - is created: by measuring and conditioning this, it is possible to get the value of current.
This device - by measuring the magnetic field - can sense DC current, AC current and even pulsed current waveform. Typically the bandwidth can go up to 1 MHz, in the best cases (for instance [8]). Galvanic insulation is guaranteed.
There are two types of this sensor: 1) open loop and 2) closed loop.

1.2.1 Open loop

In this configuration, the magnetic flux created by the primary current is concentrated in a core made with soft magnetic material: in this way almost all of the magnetic field is concentrated in the core. The magnetic field is measured by an Hall device located in an air gap (see figure 1.2). The output from the Hall device is then signal conditioned by using an operational amplifier in order to provide an exact representation of the primary current at the output. The advantages of this technology include low cost, small size and low power consumption. They are advantageous in applications where high currents (till $300A$) have to be measured. The limitations of open loop transducers are instead the poor bandwidth, the poor response time - due to the magnetic losses in the magnetic circuit - and a relatively large gain drift with respect to temperature [9].

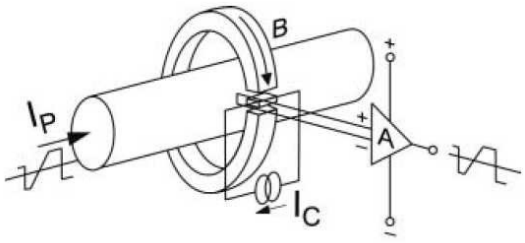

Figure 1.2: Concept of the open-loop Hall-effect based current sensor, courtesy of [9].

1.2.2 Closed loop

This configuration, called also "zero flux", is widely used thanks to its feedback configuration. Sensors in the previous measurement box [**?**] were of this type. The output Hall voltage is used as an error signal to generate a compensation current i_s in a secondary coil, in order to create a total magnetic flux equal to zero (see figure 1.3). In other words the secondary current i_s creates a magnetic flux equal in amplitude, but opposite in direction, to the flux created by the primary current. When the zero condition is established, the secondary currents is a perfect representation of the primary one and, by a shunt resistor, it's possible to handle the output as a voltage signal. The condition of zero flux reduces the drift of gain with respect to temperature; more over

bandwidth is larger, thanks to the presence of the secondary winding that acts as a current transformer at high frequency, as well as accuracy and linearity. [9]

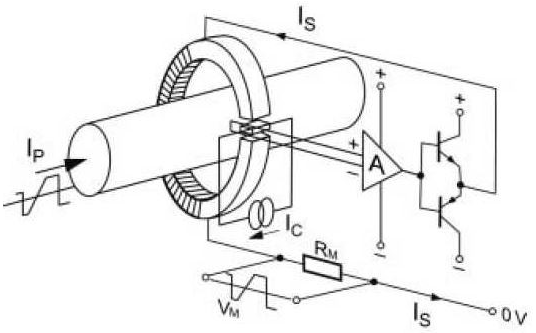

Figure 1.3: Concept of the closed-loop Hall-effect based current sensor, courtesy of [9].

Although Hall sensors are very widespread, the limitation in bandwidth - with a commercial maximum equal to 1 MHz for the sensor Allegro ACS730 [8] - represents a problem for the oversampling purpose.

1.3 Rogowski coil

Named after German physicist Walter Rogowski which proposed in 1912 the first apparatus of this kind, the Rogowski Coil is an electrical device used for measuring alternating current (AC) such as high speed transient, pulsed currents or power frequency sinusoidal currents.
The advantages of this device are multiples:

- Fast response, due to its low inductance.
- Wide bandwidth, even over 20 MHz.
- Excellent linearity, thanks to the absence of ferromagnetic material.
- Non-intrusive for the circuit and galvanic isolated, due to the geometry.

The Rogowski coil is an air core toroid, which measures EMF voltage generated by magnetic flux of a time-varying current signal. The physical principle behind the device is Faraday's law of induction, more specifically Ampère's circuital law [10]:

$$\oint (\overline{H} \cdot d\bar{s}) \approx I_{enclosed} \tag{1.3}$$

The primary current $I_1(t)$ causes therefore a flux density $B(t)$, through the magnetic field strength $H(t)$

$$\overrightarrow{B}(t) = \mu_0 \cdot \overrightarrow{H}(t) \tag{1.4}$$

and, for the Faraday's law of induction

$$\oint_c \overrightarrow{E} \cdot d\overrightarrow{s} = -\frac{d\phi}{dt} \tag{1.5}$$

a voltage, related to the time derivative of the current, is induced between the ends of the coil. By integrating this coil voltage the current is obtained.

In terms of geometry (see 1.4), the device is an helical coil of wire with the lead from one end returning through the center of the coil to the other end: both terminals are so at the same point. The coil is later wound around the conductor whose current is to be measured. The output voltage required an additional integrator circuitry.

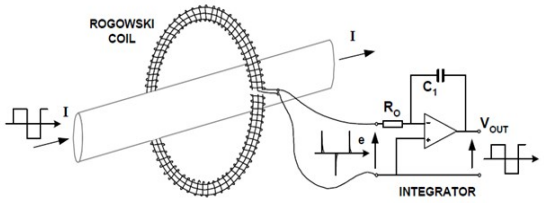

Figure 1.4: Concept of the Rogowski coil, courtesy of [11].

The mutual inductance M of each turn determines the magnitude of induced voltage, modeled as a voltage source [10]:

$$u_{induced}(t) = -M\frac{di_1(t)}{dt} \tag{1.6}$$

The circuital model includes also the resistance and the self inductance: indeed one important design consideration is the resonance frequency, which determines the bandwidth.

Although the many advantages, there is an issue. The basic principle of Rogowski coil is based on the detection of a flux change, which is proportional to a current change: it's thus unattainable to reconstruct a DC component.
For the set up under consideration, it is impossible to overlook this aspect since the measurement of the DC component must be available for a variety of reasons relating to control purposes:

- DC currents are set when the rotor of a rotating machine should be locked in a certain position. Therefore, the DC currents must be measured in the case of a closed-loop control.
- In synchronous machines, some sensor-less algorithms for zero-speed require the use of DC currents.
- By a super-imposition of a DC current over an alternate one, the stator resistance can be evaluated.
- The effects that the dead times produce on the applied voltages can be assessed by measuring the DC current.

1.4 HOKA principle

The HOKA principle combines two different types of current sensors: one Rogowski coil with four Hall or magneto-resistive sensors. For further details on the latter type of sensor, please refer to the following section 2.

The frequency behavior of a Rogowski coil can be approximated by an high-pass transfer function, while that of magneto-resistive sensor gets closer to a low-pass. By analog processing and matching these two signals, it's possible to obtain - theoretically - a very high bandwidth [12].

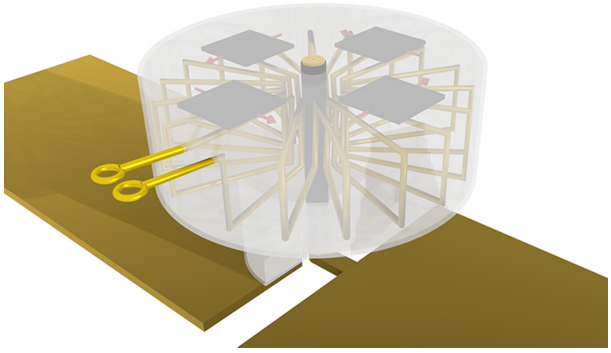

Figure 1.5: Conceptual design of the current sensor designed with Hoka principle [12].

The mechanical arrangement, according to [12], should be a coaxial set up: by doing so the insertion inductance is low, in the area of a few nH, and the magnetic field is proportional to the current (see figure 1.5).
The device is inserted into the current path. Each of the four magneto-resistive sensors (the square-shaped plates in the figure 1.5) consists of two ferromagnetic layers separated by a thin isolator and arranged in a bridge circuit configuration, symmetrically around the middle hole.

The magneto resistive effect could work theoretically from DC up to several MHZ range but in practice parasitic effects limit the frequency domain. For further details on this principle, please refer to the following section (2).

The Rogowski coil, already discussed in the previous point, works in the range of high frequencies. As explained above the two sensors signals have to be matched to get a flat frequency response (see figure 1.6). If necessary, it is possible to insert a low-pass filter of the first order according to the system requirements.

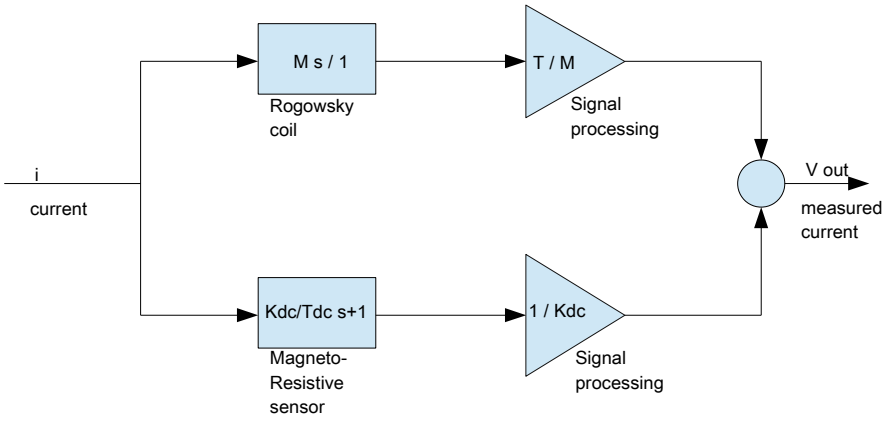

Figure 1.6: Block diagram of the HOKA principle [12].

This technology, exceptionally suitable for a huge bandwidth, has not yet been developed for the market. Its complexity represents, *ça va sans dire*, an obstacle and solutions available on the market are preferred.

1.5 Current Viewing Resistor (CVR)

The simplest solution in current sensing field is shunt resistor. It consists of a current-to-voltage converter, where a resistor is inserted in the current path and thus the current is converted to voltage in a linear way by the classical Ohm's law:

$$v = R \cdot i \tag{1.7}$$

Some benefits of this technique are its simplicity, low cost and a reasonable accuracy. At the same time, there is no galvanic protection and the small voltage drop across the resistance needs amplification, which alters bandwidth and performances, as well as increases the device cost.

Power converters, more-over, have reached a power density level where the power losses inside shunt resistors start to become troublesome; therefore, the research on power electronics is focusing on alternatives for shunt resistors with similar accuracy but lower losses and with an output voltage that can be directly sampled by an analog-to-digital converters [13].

Another aspect to take into account is the rejection to common-mode. The common mode voltage at the input of an operational amplifier is defined as

$$\frac{V_1 + V_2}{2} \tag{1.8}$$

Changes in common mode voltage will produce changes in output. It would be desirable that if a signal is applied equally to both inputs of an op amp, so that the differential voltage is unaffected, the output should not be affected as well [14]. The common-mode rejection ratio (CMRR) is the ratio of common-mode gain to differential-mode gain. It is often expressed in dB.

For motor drive application where the measurements are picked in the inverter - motor line (figure 1.7), the common mode input voltage of op amps present within current sensors must be high. In the present case, the voltage required from a CMRR point of view is equals to 560 Vdc.

Nevertheless these last aspects concerning power losses and flexibility, the theoretically very high bandwidth makes this simple method remarkable - for oversampling purpose - among the various possibilities.

In particular, the design of Texas Instrument "TIDA-00445" [15] (see figure 1.7) has been studied for numerous similarities with our system, above all configuration and current range.

The system includes a shunt, a gain-stage using two precision op amps (OPA2376 [16]), a reinforced isolation amplifier (AMC1301 [17]) and a differential to single-ended conversion using the OPA376 [16].

The shunt should drop a voltage of 25 mV across it when carrying 200 A: a shunt value of 125 $\mu\Omega$ is required, with a required minimum power capability of 5 W.

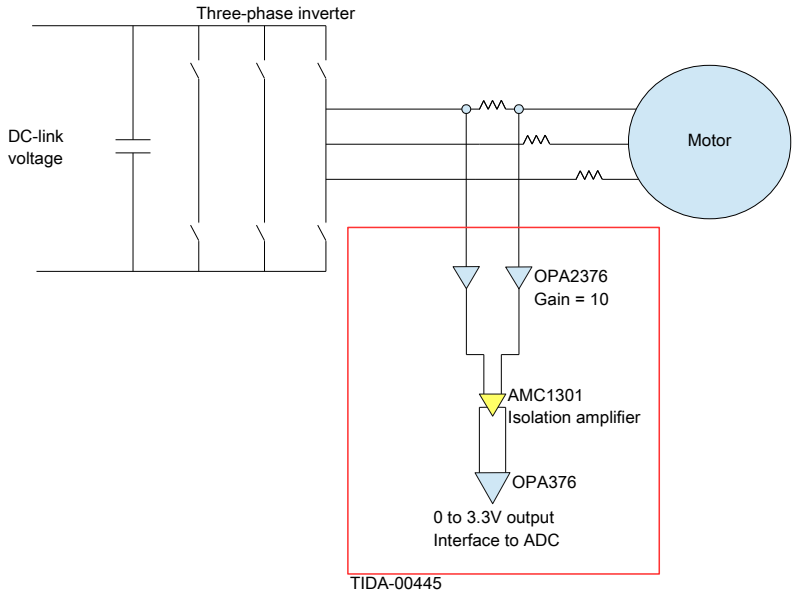

Figure 1.7: Concept of the "TIDA-00445" [15].

OPA2376 are used in an instrumentation amplifier topology (see figure 1.8) and allow to amplify the ±25 mV across the shunt to ±250 mV to fit the input range of the isolation amplifier. The gain of this first stage is therefore equal to 10.

The following stage involves AMC1301, which provides a gain of 8.2 as well as galvanic isolation between high and low voltage circuit of up to 7000 V_{peak}. Finally, the precision op amp OPA376 permits to match the signal with the input range of the single-ended analog-digital converter (mapped approximately 0 V to 3.3 V).

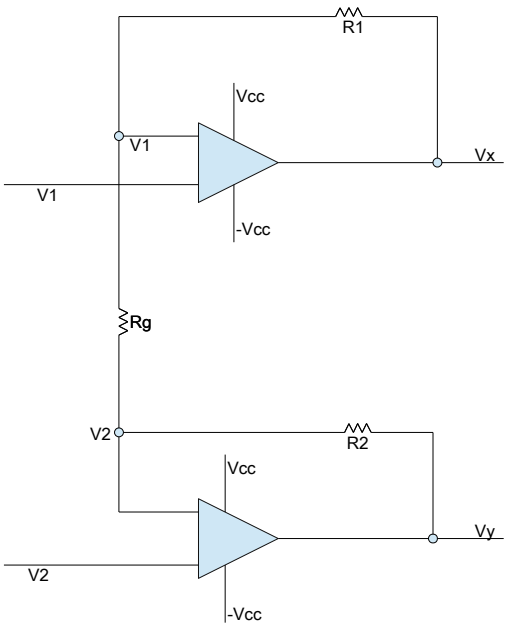

Figure 1.8: Instrumentation amplifier stage with two OPA2376.

In the figure 1.9 the practical implementation of the "TIDA-00445" is shown.

This solution is eventually shelved for a bandwidth reason. This parameter, in this design, is uniquely determined by the four op amps (figure 1.7) and the isolation amplifier AMC1301 according to the data sheet [17] has a bandwidth equal to 200 kHz, certainly too few for oversampling purposes.

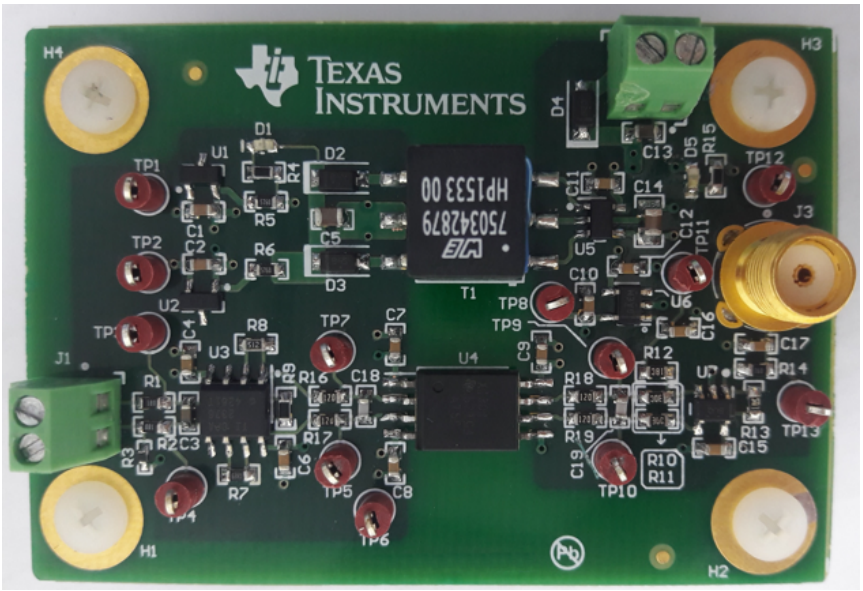

Figure 1.9: Practical implementation of the "TIDA-00445" [15].

Chapter 2

Sensitec CMS3050

In this section the magneto-resistive current sensor "Sensitec CMS3050" is explained. Starting from the underlying physical principle and the reasons why the sensor is chosen, features and parameters are reviewed.

2.1 The magneto-resistive effect

In thin films of some material, for instance permalloy (a nickel (80%) - iron (20%) magnetic alloy) the electrical impedance changes when an external magnetic field is applied in the plane of the film. The variation is due to the rotation of film magnetization; if the magnetic field is external, the effect is called anisotropic magneto resistive (AMR) effect. It was first discovered in 1857 by Lord Kelvin.

In the four permalloy strips (cerulean color in the figure 2.1), the resistance changes in a proportional way to the applied magnetic field. By adopting a proper design, small magnetic fields can be detected with very high accuracy: there is no need to use an iron core to concentrate the magnetic field generated by the conductor carrying current, avoiding thus the disadvantages of hysteresis. Galvanic isolation and low power losses are others advantages of this technique [5].

A MR current sensor works with a differential field measurement with compensation.

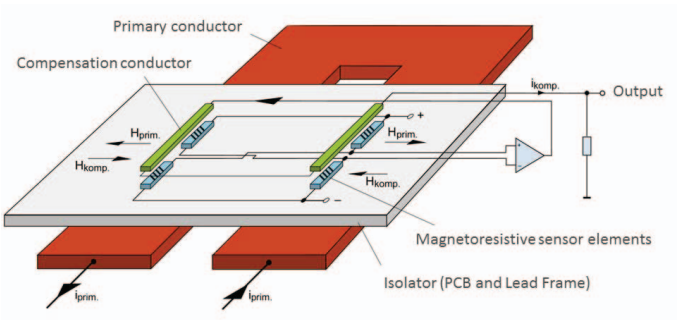

Figure 2.1: Principle of a magneto - resistive current sensor [5].

The primary current conductor is U-shaped, positioned underneath the sensor. The chip is assembled on a ceramic substrate. Four AMR resistors are connected to form a Wheatstone bridge and are combined with a signal conditioning circuit.

This last generates a current i_{comp} in the compensation conductor, which compensates the magnetic field generated by the primary conductor in the permalloy strips

plane. i_{comp} is directly proportional to the current to be measured and is used to generate the output voltage signal.

The declared range bandwidth is from DC to 2 MHz, when the output of the sensor is filtered with an on-board RC filter. From the figure 2.2 which reports the bode diagram of the magnitude of the unfiltered and filtered sensor output, it is visible that bandwidth of the unfiltered signal might be extended further since the harmonic content increases in amplitude for high frequencies. Thus the magneto-resistive sensor, with a proper improvement in terms of bandwidth, represents a suitable compromise for oversampling purposes (see figure 2.3).

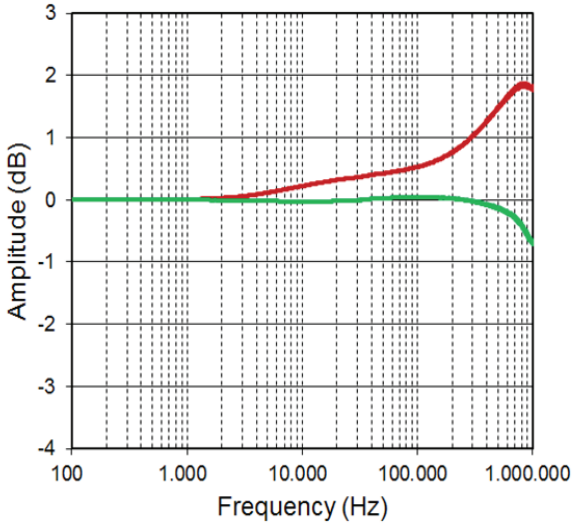

Figure 2.2: Frequency response of the device with RC-filter (green) and without (red) [18].

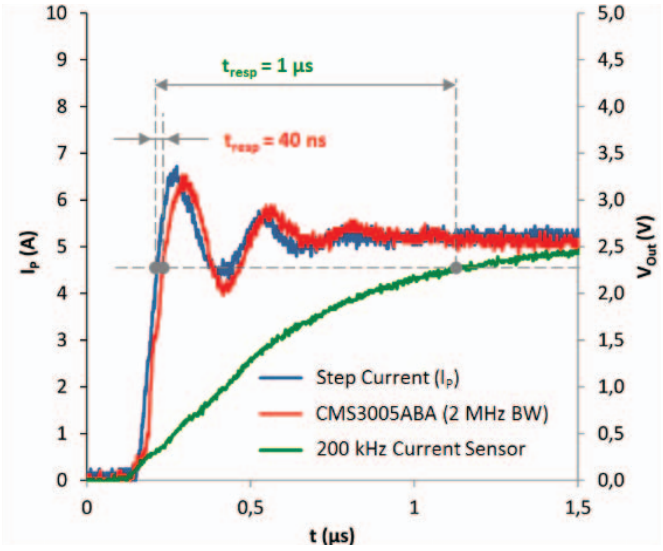

Figure 2.3: Step response of the device [18].

2.2 Data of CMS3050

Among magneto-resistive current sensor family the Sensitec CMS3050 is chosen [18]. In the following table 2.1 the main features are resumed.

Parameter	**Min**	**Max or typical**
Supply voltage	±12 V	±15 V
Primary measuring range	- 200 A	+ 200 A
Primary nominal current I_{PN}		50 Arms
Frequency bandwidth (- 3 dB)	2 MHz	
Accuracy (as % of I_{PN})		±0.8
Nominal output voltage V_{outN} with I_{PN}		2.5 Vrms
Output gain between I_{outN} and V_{outN}		1/20
Nominal current consumption		50 mA
Maximal current consumption, within the measuring range		110 mA
Maximal current consumption, outside the bounds		105 mA
Internal burden resistor for output signal R_M		126 Ω
Rise time, from 10 %I_{outN} to 90 %I_{outN}		0.05 μs
Response time, from 90 %I_{PN} to 90 %I_{outN}		0.04 μs

Table 2.1: Electrical data of the Sensitec CMS3050.

Sensitec GmbH offers the possibility to buy, together with the sensor, an evaluation board ready for use [19], whose dimensions are 75 mm in width and 90 mm in length. In this way the current to be measured can be directly connected via screw connectors to a busbar. On the secondary side, there are three output signals available, both as screw terminals to connect to the board and test pins: an unfiltered output voltage, a pre-assembled filtered output voltage and a customized filtered output voltage.

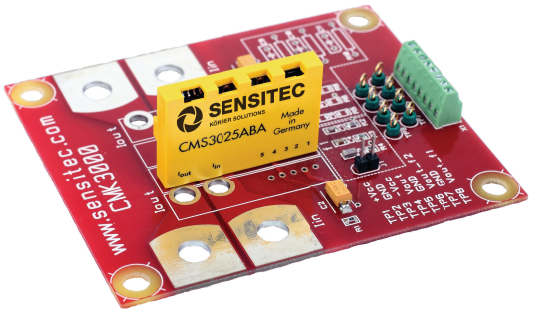

Figure 2.4: The CMK3000 board: in yellow the current sensor [18].

Since the maximum bandwidth is not declared in the data sheet, the following step has involved the assessment of the frequency response. Once the bandwidth is known, it is possible to think about the board design upgrade.

Chapter 3

Current sensor filtering

In this section the sensor is tested in order to verify its dynamic response. This first investigation is performed in the time domain, where a proper analog filter at the output of the unfiltered voltage is used to increase the declared bandwidth of the sensor.

3.1 Introduction

The frequency response of a system $G(j\omega)$ - in our case a sensor - is the complex ratio of the output and the input of the system. It is expressed as function of frequency and it is used to characterize the dynamics of the system in terms of spectrum.

Briefly, if a signal is injected into a system at a given frequency, the system (represented in the figure 3.1) will respond at the same frequency with a certain magnitude and a certain phase shift relative to the input. Repeating this test for different values of frequency (sweep), the frequency response can be plotted.

Assuming two I/O sinusoidal signals where $u(t)$ is the input and $y(t)$ is the output,

$$u(t) = A \cdot \sin(\omega t + \varphi) \tag{3.1}$$

$$y(t) = B \cdot \sin(\omega t + \Upsilon) \tag{3.2}$$

the relation between them is

$$B = A \cdot |G(j\omega)| \tag{3.3}$$

$$\Upsilon = \varphi \cdot \angle G(j\omega) \tag{3.4}$$

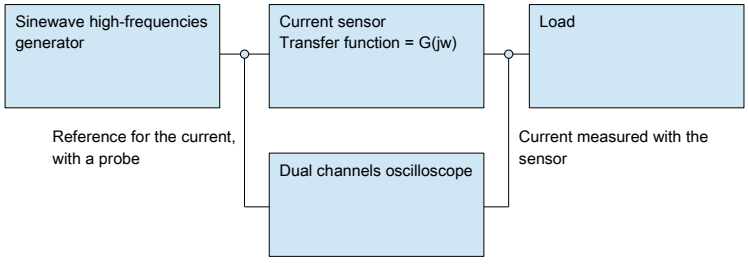

Figure 3.1: Ideal set up to detect the frequency response.

This comparison is often made through a process known as Fast Fourier Transform (FFT), an algorithm that samples a signal over a time period and it divides into its frequency components by a Fourier analysis.
The frequency response consists of two parts: the system's response magnitude, measured in dB, and the phase, measured in radians. These two are typically plotted in two rectangular plots as functions of frequency, obtaining thus a Bode plot.

Knowing the frequency response makes feasible to find the current sensor bandwidth and, consequently, the harmonic content available for oversampling purpose.

3.2 Testing Signal Generator Agilent Tech 33120A

A first test is performed using a 15 MHz synthesized function generator, the Agilent 33120A [20] (front panel in figure 3.2), connected with a 50 Ω resistance load. Two probes are connected, one for the voltage and one for the current. The purpose of the test is to detect the behavior of current and voltage at high different frequencies, evaluating if the amplitude is in a sufficient resolution to test later on the current sensor.

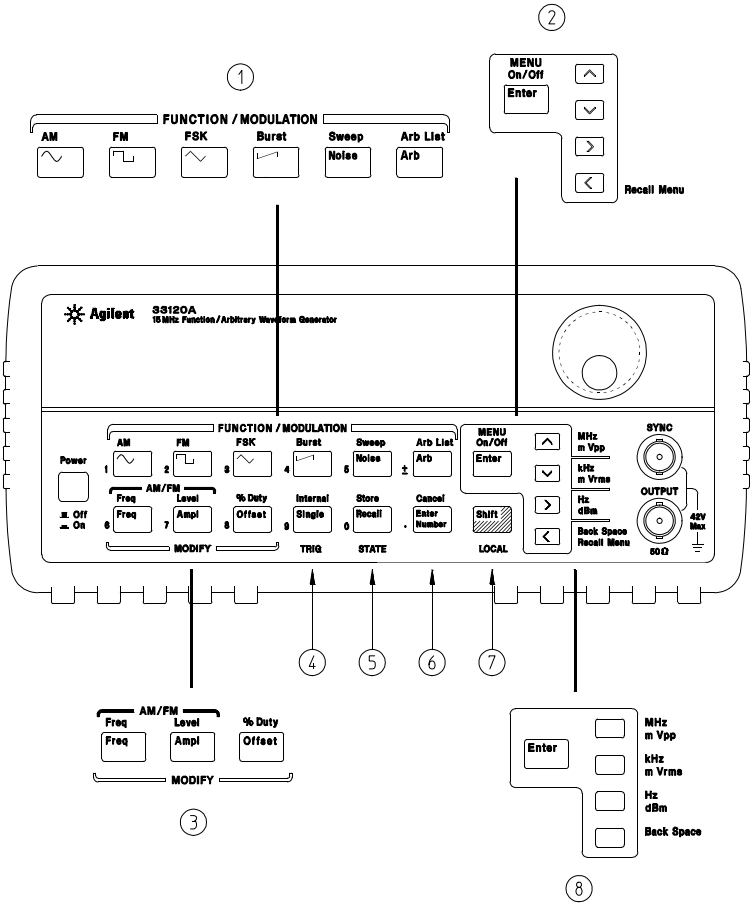

Figure 3.2: The front panel of the Agilent 33120, [20].

The theoretical peak to peak voltage supplied by the signal generator is:

$$V_{pp} = 5V \tag{3.5}$$

and consequently the current, in a 50 Ω load was:

$$I_{pp} = 200mA \tag{3.6}$$

In the following table measurements are reported.

$Freq[Hz]$	$I_{RMS}[mA]$	$V_{RMS}[V]$	$\|Z\|[\Omega]$	$Phase-shift[degree]$
50	70.614	1.750	24.78	+7.2
100	69.881	1.751	25.06	+3.6
200	69.826	1.75	25.06	+1.5
300	69.679	1.748	25.09	+1.4
400	69.664	1.747	25.10	+1.2
500	69.505	1.745	25.11	+1.2
1 k	69.399	1.733	24.97	-1.3
10 k	69.401	1.685	24.28	-2.4
100 k	68.641	1.702	24.80	-4.3
500 k	68.067	1.766	25.95	-20.9
1 M	64.169	1.944	30.30	-38.2
2 M	59.266	2.161	36.46	-50.8
3 M	42.972	2.616	60.88	-72.4
4 M	33.724	2.718	80.60	-80.7
5 M	26.216	2.715	103.56	-86.4

The outcomes show that:

- Current drops from the initial value of 70 mA to 25 mA.
- Voltage rises from the initial value of 1.75 V to 2.75 V.
- Impedance rises from the initial value of 25 Ω (resulting from the parallel of the 50 Ω load plus the internal load of 50 Ω) to 100 Ω.
- Phase shift changes from the initial inductive behavior (+10°) to a complete capacitive behavior (-90°).

In the figure 3.3, the current detected with the scope at 5 MHz is showed.

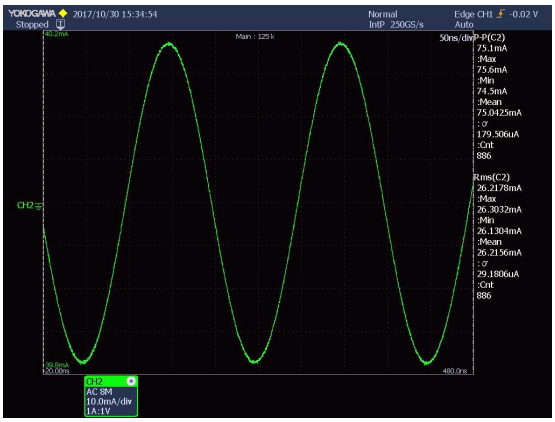

Figure 3.3: Current on the 50 Ω resistance at 5 MHz.

Sensitec CMS3050 (see the data sheet [18]) has an output of 2.5 V when it measures the nominal current of 50 Arms. The gain of the device is therefore 1/20. Testing the current sensor with Agilent 31022 would have meant to obtain, at 5 MHz, a primary current equals to 25 mArms and so a voltage output signal of 1.3 mV. The noise level (RMS) of the device is equal to 0.25 mV (see [18]), almost 20% of the signal.

Therefore, the amount of current available with Agilent 31022 is too weak to make an accurate comparison. Decreasing the resistance (f.i. 1 Ω), in order to have more

current, is not feasible since the fuse inside the signal generator stops currents greater than 500 mA.

A possible alternative is to build a resonant circuit, inserting an inductance in parallel and tuned on the desired frequency. This can theoretically boosts current by the magnifying factor Q but, at high frequency (f.i. 5 MHz), a simple inductance introduces some parasitic capacitances as well.

Audio generators on the market may reach high frequency but at the same time they do not possess a large current magnitude. An alternative is sought.

3.2.1 Investigation of a proper set up: Brockhaus MPG 200D AC/DC

A signal able to run into the domain of high frequency with a fair current amplitude is required. Brockhaus MPG 200D AC/DC is a test bench for the measurements of magnetic proprieties of materials. Embedded with the device there is one wave form generator, with two stages of power amplifiers. The maximum frequency using this last is equal to 20 kHz (fundamental) for PWM signals, with a maximum declared current of 50 A, using the second stage amplifier.

Even exploiting harmonics in the high frequency domain, the combination of frequency/amplitude is still feeble.

3.2.2 Investigation of a proper set up: IGBT short circuit tests

A short circuit test on IGBT modules permits to assess the capability of IGBT to withstand extremely severe condition. By doing this, IGBTs can switch in some case with a significant slew rate (13 kA/μs). Theoretically, it is possible to use this signal in order to develop a large harmonic content to inject in the current sensor.
The double switching on/off of an IGBT can be approximate to a triangular pulse. Assuming a slew rate of 12.5 kA/μs means a rise time (0 - 50 A) of 4 ns. In the following figures 3.4 and 3.5 the pulse and its FFT are shown.

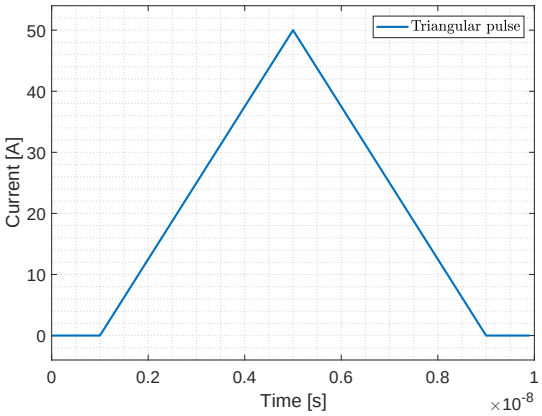

Figure 3.4: Triangular pulse

Building a new set up is possible, but with evident complexities: a switching time of 4 ns is not possible with off-the-shelf components, fast switches (e.g. SiC MOSFET) can achieve in best cases 50 ns, with a trapezoidal-shape signal. The construction of a new set up, more-over, requires more time that the available one. The easy trade off is found in using inverter-fed motors already in place in the laboratory.

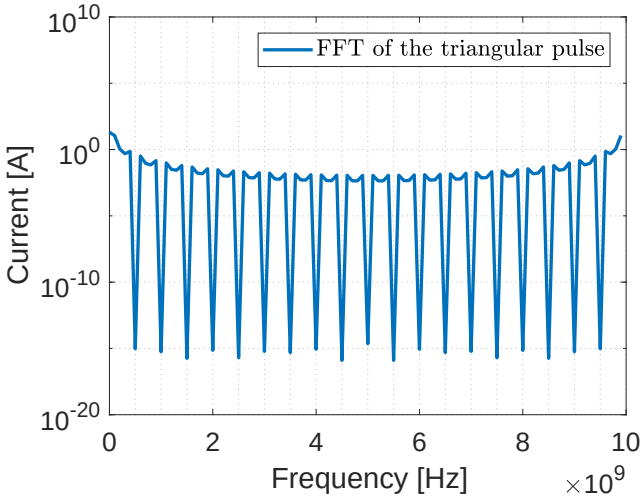

Figure 3.5: FFT of the triangular signal

3.3 Test on Inverter-fed SynRMs

The experiments are carried in the Motor Lab, in the ABB Corporate Research in Västerås, Sweden. The first part involves the choice of the best motor in terms of harmonic content: that means, paradoxically, to identify the most aged machine.

The second part concerns instead the elaboration of data in order to find a proper filter.

Two synchronous reluctance motors are fed by an inverter controlled by a scalar PWM. With a probe, one current phase is detected. Two observation windows are chosen: one long (1 sec) and one short (0.2 msec). The following pictures 3.6 and 3.7 show the measurements for one machine.

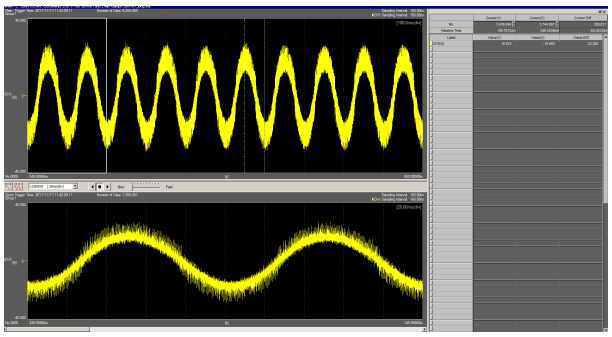

Figure 3.6: Current of one phase, in a 1 second window, of the SynRM 15kW.

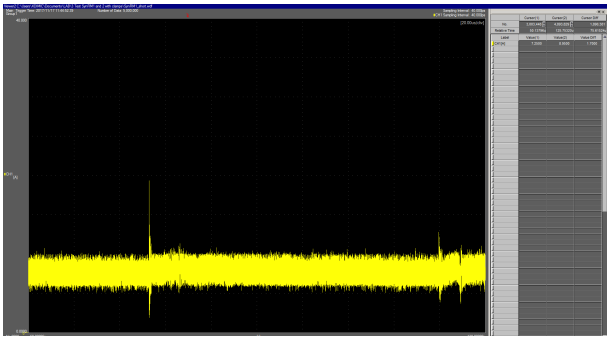

Figure 3.7: Current of one phase, in a 0.2 millisecond window, of the SynRM 15kW. The switching instant is visible.

With a post-processing elaboration in Matlab, a narrow time window is taken (figure 3.8) and the FFT is developed (figure 3.9).

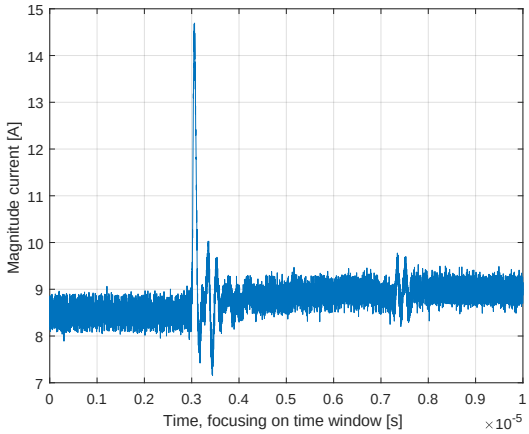

Figure 3.8: Current of one phase, in a 10 microseconds window, of the SynRM 15kW. The switching event is visible.

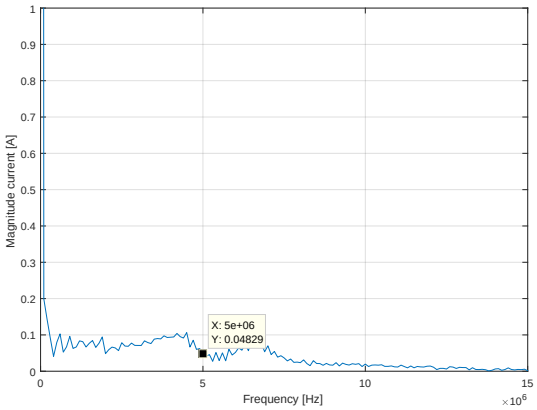

Figure 3.9: FFT of the signal: the cursor points at 5 MHz.

The figure 3.9 shows that short interval means more magnitude in frequency but, at the same time, less resolution in the frequency domain.

The 11 kW motor presents more noise and disturbances and so an higher harmonic content and it is therefore chosen for the subsequent trials. Another test is carried: the current sensor is connected in one phase of the inverter-motor line. One current clamp and two voltage probes are arranged in different position:

- channel 1 - yellow trace: positioned in the line motor-inverter. This measurement represents the actual current i_a, unaffected by the current sensor and measured with a high-bandwidth (100 MHz [21]) current clamp.
- channel 2 - green trace: positioned in the test pin on the board CMK3000 (see fig. 2.4). This measurement, performed by a voltage probe, represents the unfiltered current of CMS3050 $i_{a,unfiltered}$.
- channel 3 - pink trace: positioned in the test pin on the board CMK3000 (see fig. 2.4). This measurement, performed by a voltage probe, represents the pre-assembled RC filtered current of CMS3050 $i_{a,filtered}$.

The machine is then fed by the inverter.

Make a comparison with different TFs is problematic because of the noise present in the system. A time domain is therefore selected in order to build the best analog filter to apply at the sensor in order for the green curve - unfiltered current - to follow the yellow one - actual current - as close as possible. As matter of fact, detecting the current at the switching instant and then building a proper filter around it, allows to achieve the suitable filter and time response.

In the following figures 3.10, 3.11 and 3.12 different time windows are shown.

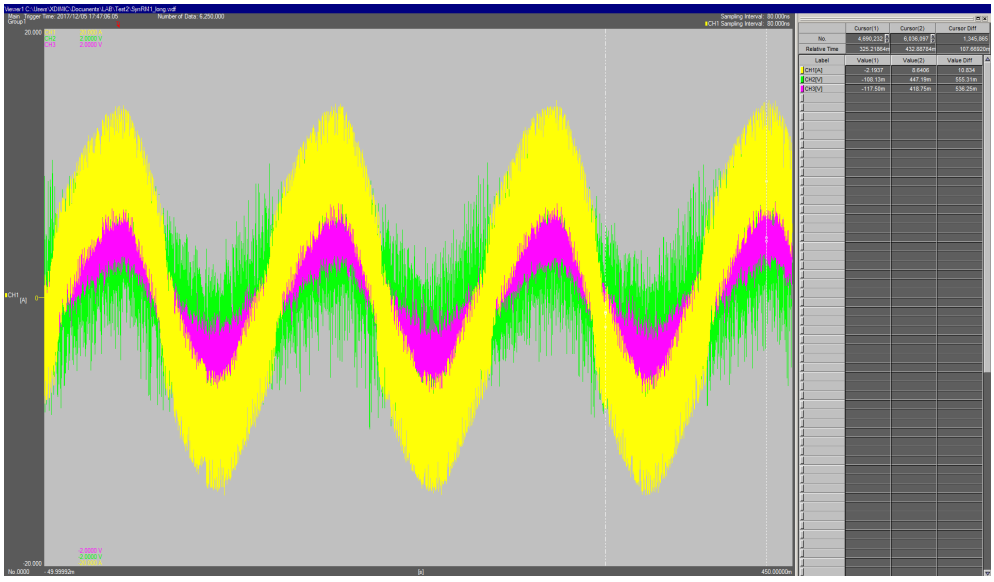

Figure 3.10: Current of one phase detected by three clamps, 1 second window observation, SynRM 11kW.

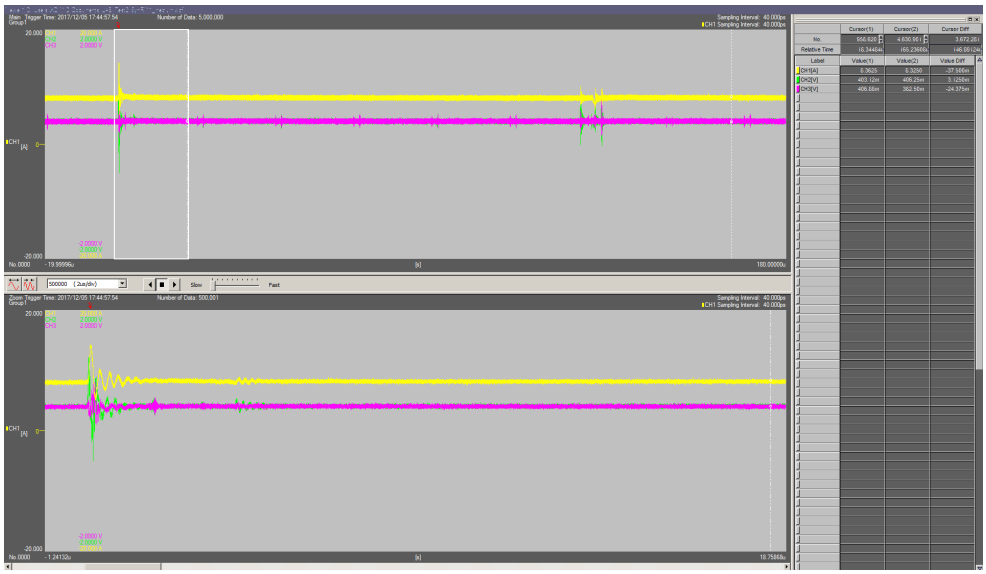

Figure 3.11: Current of one phase detected by three clamps, 0.2 milliseconds window observation, SynRM 11kW. It is visible, zoomed, the switching instant.

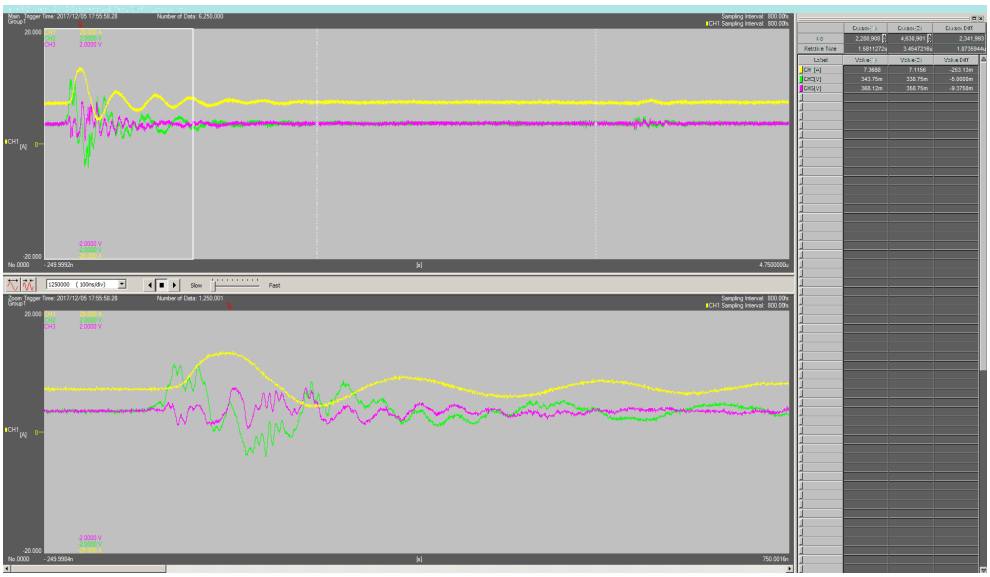

Figure 3.12: Current of one phase detected by three clamps, 5 microseconds window observation, SynRM 11kW. It is visible, zoomed, the switching instant.

The oscilloscope data are then elaborated in Matlab, with the aim of finding out a transfer function - representation of a filter - able to follow the signal. Assuming as input $i_{a,unfiltered}$ and as output i_a, the transfer function is estimated with the command *"tfest"*, which permits to define the number of poles and of zeros of the TF.

A model in Simulink (see figure 3.13) allows to compare i_a with $i_{a,unfiltered}$ combined with the filter.

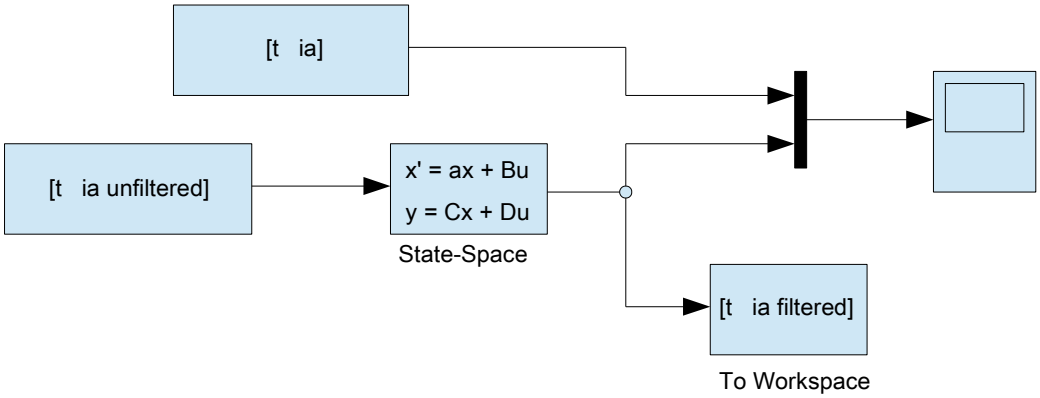

Figure 3.13: Simulink model that compares i_a with $i_{a,unfiltered}$ plus the filter (block State-Space).

In the following figures 3.14, 3.15 and 3.16, some elaborations are shown. The actual current i_a is printed in blue, while the $i_{a,filtered}$, made by the chain of $i_{a,unfiltered}$ and the filter, is printed in orange.

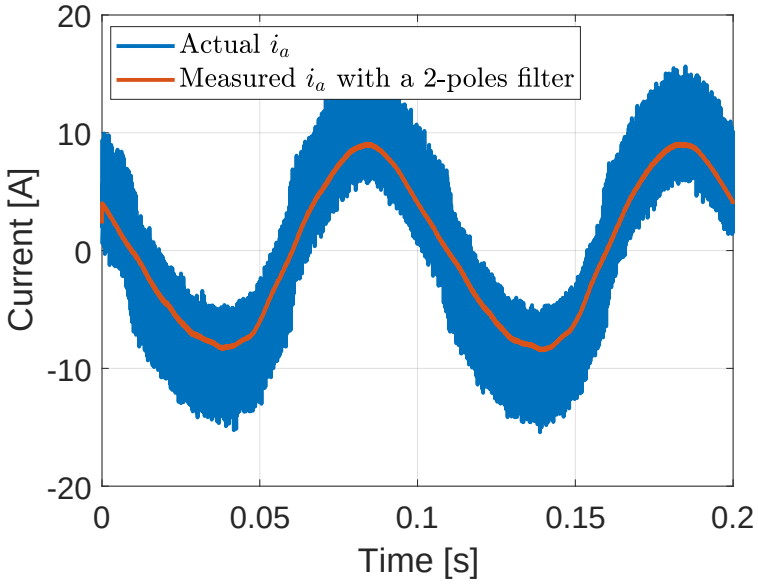

Figure 3.14: Processed-data in a 0.2 s window, transfer function estimated with two poles.

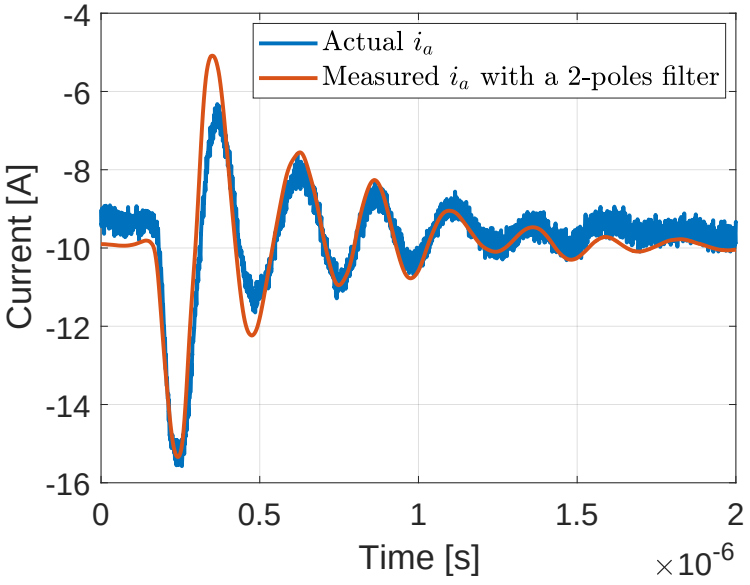

Figure 3.15: Processed-data in a 2 us window, transfer function estimated with two poles.

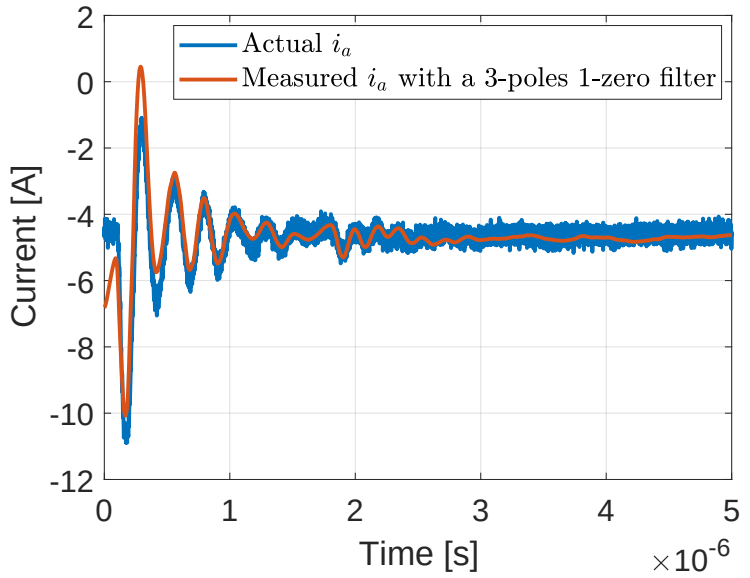

Figure 3.16: Processed-data in a 5 us window, transfer function estimated with three poles and one zero.

The so-simulated filters can follow the actual current.

Another comparison method is made using the Matlab application *"System Identification"*. This allows to insert I/O data in order to estimate a transfer function specifying poles and zeros.

In the following figures 3.17 and 3.18, some elaborations are shown.

```
>> tf2

tf2 =

  From input "ia_unfiltered" to output "ia":
           5.086e14
  ---------------------------
  s^2 + 3.606e07 s + 4.794e14

Name: tf2
Continuous-time identified transfer function.

Parameterization:
   Number of poles: 2   Number of zeros: 0
   Number of free coefficients: 3
   Use "tfdata", "getpvec", "getcov" for parameters and their uncertainties.

Status:
Estimated using TFEST on time domain data "filterTARGET".
Fit to estimation data: 54.29% (stability enforced)
FPE: 0.3373, MSE: 0.3373
>> 2e7/(2*pi)

ans =

   3.1831e+06
```

Figure 3.17: Numerical value of an estimated transfer function with *"System Identification"*.

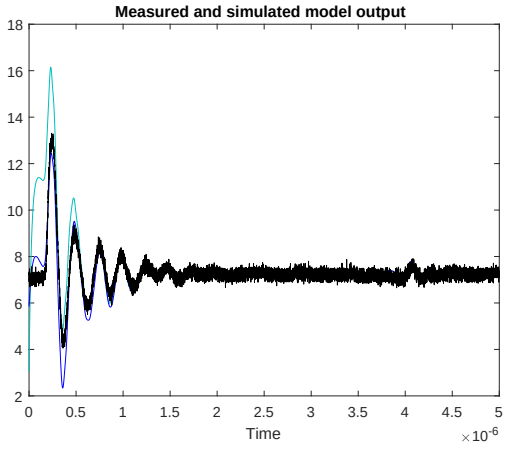

Figure 3.18: Processed-data in a 5 us window, multiple transfer-functions estimated with *"System Identification"*: blue one with 2-poles, cerulean one with 3-poles 1-zero.

The analysis show that adding poles and zeros above and beyond does not improve the accuracy. Therefore it is preferable to use a two-poles analog filter: the constructive complexity is reduced.

At that point, a comparison with different transfer functions is run. Each TF represents a filter. In the following table 3.1 only the four best solutions are resumed. For the sake of completeness all the TFs used are reported in the appendix A; for an in-depth explanation of the filters please instead refer to the next section 3.4.

Filter-type	**Numerator**	**Denominator**	**Cut-off frequency**
$Bessel, M-FB$	$1.4e15$	$s^2 + s \cdot 33.3e6 + 3.6e14$	$2.3MHz$
$Butterworth, M-FB$	$1.5e15$	$s^2 + s \cdot 27.3e6 + 3.7e14$	$3MHz$
$Bessel, Sellen-Key$	$2.3e15$	$s^2 + s \cdot 41.4e6 + 5.7e14$	$3MHz$
$Butterworth, Sellen-Key$	$1.4e15$	$s^2 + s \cdot 26.6e6 + 3.5e14$	$3.4MHz$

Table 3.1: Features of the four transfer functions used.

With the Simulink model (see figure 3.13), the two signals i_a and $i_{a,filtered}$ are tested for all the measurements and then the Root-Mean-Square Deviation (RMSD) is computed:

$$RMSD = \sqrt{\frac{\sum (i_a - i_{a,filtered})^2}{N}} \cdot \frac{1}{i_{a,RMS}} \tag{3.7}$$

The mean of the RMSDs, calculated for each measurement, shows that filters have almost the same error.

Filter-type	**RMSD**
$Bessel, Multiple-Feedback$	10.53
$Butterworth, Multiple-Feedback$	11.15
$Bessel, Sellen-Key$	11.78
$Butterworth, Sellen-Key$	10.93

With the aim of improving the accuracy of the simulation, the same filters are made digital with the Matlab command *"c2d"*. The results are reported:

Filter-type	**RMSD**
$Bessel, Multiple-Feedback$	12.29
$Butterworth, Multiple-Feedback$	12.03
$Bessel, Sellen-Key$	12.48
$Butterworth, Sellen-Key$	12.03

Digitalization adds more noise but solely in a range of 1%.

Last elaboration concerns the addition of noise with the Matlab command *"awgn"*. Results are reported:

Filter-type	**RMSD**
$Bessel, Multiple-Feedback$	36.73
$Butterworth, Multiple-Feedback$	37.33
$Bessel, Sellen-Key$	37.49
$Butterworth, Sellen-Key$	37.30

Last values confirm the obvious fact that inserting a white noise carries a significant growth in terms of error. Nevertheless the filters can still roughly follow the input signal.

3.4 Choice of the analog filter

The analog filter theory [22] has been studied in order to choose the best design solution. The main requirement is a large bandwidth to detect the current high frequency behavior. The approximation should be a low-pass filter since the sensors must be able to measure both DC and AC currents.

A second-order low-pass filter has a pair of complex conjugate poles on the left side of the S-plane. S-plane is the complex plane on which Laplace transforms are graphed: the real-axis, horizontal, is denoted by σ while the imaginary-axis, vertical, is denoted by ω.

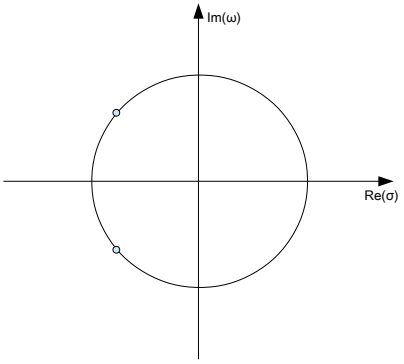

Figure 3.19: Pole location in S-plane: the choice of left side is due to stability.

The typical Bode diagram of a low pass filter is:

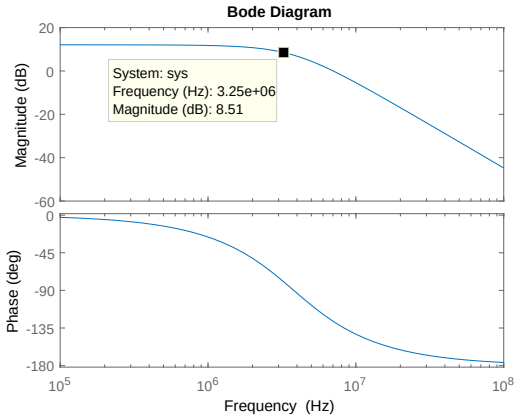

Figure 3.20: Bode diagram of a second-order low-pass filter.

The transfer function of a second order low-pass filter is:

$$H(s) = \frac{G}{s^2 + \frac{\omega_0}{Q} \cdot s + \omega_0^2} \tag{3.8}$$

where G is the gain, Q is the quality factor of the filter and $\omega_0 = 2 \cdot \pi \cdot f_{cutoff}$ is the cut-off angular frequency (in rad/sec).

Two typologies of filters related to two topologies have been examined.

3.4.1 Butterworth

This response is one of the best known and one of the most widely used at once. It has no ripple neither in the pass band nor in the stop band; because of this is termed maximally flat filter. At the same time the response exhibits a poor roll-off rate, compared to others filters not taken into account in this analysis (f.i. Chebyshev or Elliptic).

The transient response of a Butterworth filter to a pulse input shows moderate overshoot and ringing and the quality factor Q is equal to 0.707. The values of the elements of this filter are more practical and less critical than other filter types.

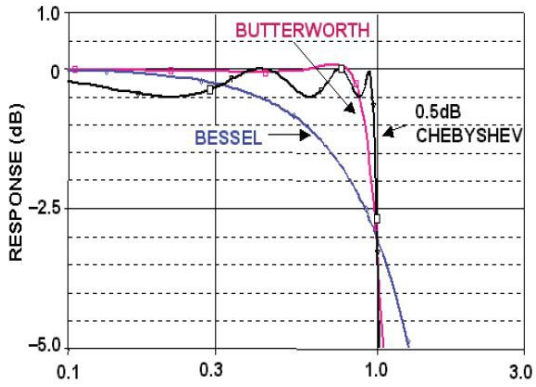

Figure 3.21: Comparison of magnitude bode diagram: Chebyshev has not been dealt with in the report [22].

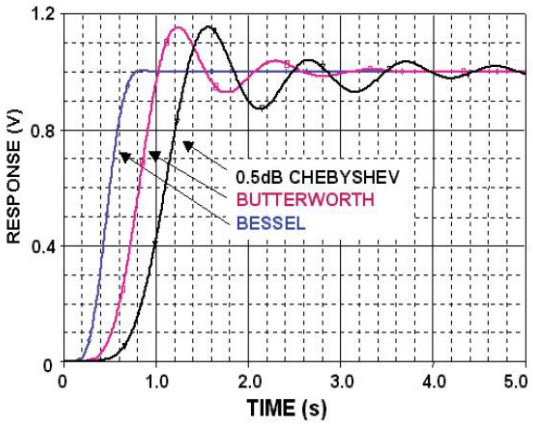

Figure 3.22: Comparison of step response: Chebyshev has not been dealt with in the report [22].

3.4.2 Bessel

The Bessel has the best phase response, even better than the Butterworth. The Bessel filter achieves this flatness at the expense of the roll-off rate, which is the slowest one among the other filters.

This solution, more-over, shows the best behavior in the time domain (figure 3.22) [22]. Indeed the impulse response of a filter (and so the step response, integral of

the last one), in the time domain, is proportional to the bandwidth in the frequency domain. The narrower the impulse, the wider the bandwidth of the filter.

The quality factor Q is equal to 0.577. The frequency scale factor (FSF) is defined - in the Sallen-Key configuration - as:

$$FSF \cdot f_{cutoff} = \frac{1}{2 \cdot \pi \cdot \sqrt{R_1 \cdot R_2 \cdot C_1 \cdot C_2}} \tag{3.9}$$

The Butterworth filter has FSF equal to 1 - as it was already said this typology of response has an inherent simplicity. For a Bessel instead the FSF is equal to 1.274.

3.4.3 Sallen-Key configuration

This configuration, termed also voltage control voltage source (VCVS), is one of the most widely used. Its popularity is due to its least dependence on the op amp performance, that is not configured as an integrator but as an amplifier: this leads to a minimization of the op amp gain-bandwidth requirements. In this way the filter can work till higher frequency compared to other topologies. In the following figure 3.23 a second order low pass Sallen-Key configuration is shown.

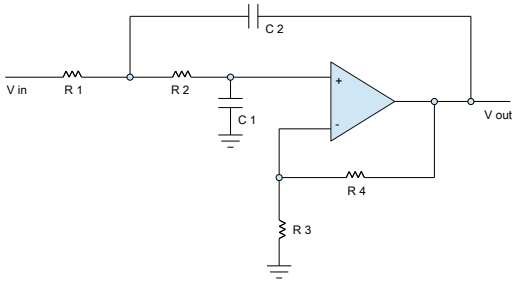

Figure 3.23: Second order low pass active filter in the Sallen-Key configuration.

The ideal gain of a low-pass filter in Sallen-Key architecture is:

$$K = \frac{R_3 + R_4}{R_3} \tag{3.10}$$

while the cutoff frequency is:

$$FSF \cdot f_{cutoff} = \frac{1}{2 \cdot \pi \cdot \sqrt{R_1 \cdot R_2 \cdot C_1 \cdot C_2}} \tag{3.11}$$

3.4.4 Multiple-Feedback configuration

In this architecture the op amp is used as an integrator, as shown in the figure 3.24. In this case the dependence of the transfer function to the op amp performance is substantial. Working at high frequencies results consequently harder due to the limitations of the open-loop gain of the op amp. More-over the multiple feedback configuration will invert the phase of the signal.

The ideal gain of a low-pass filter in Multiple-Feedback architecture is:

$$K = -\frac{R_2}{R_1} \tag{3.12}$$

while the cutoff frequency is:

$$FSF \cdot f_{cutoff} = \frac{1}{2 \cdot \pi \cdot \sqrt{R_2 \cdot R_3 \cdot C_1 \cdot C_2}} \tag{3.13}$$

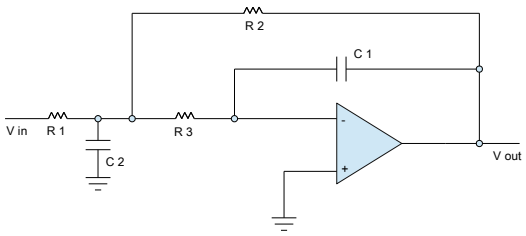

Figure 3.24: Second order low pass active filter in the Multiple-Feedback configuration

3.5 Design of the analog filter

Considering the analysis carried out above, a Bessel filter is chosen because it shows the best behavior in the time domain. Sallen-Key configuration instead is chosen thanks to the least dependence on the op amp performance.

For the practical design, two on-line softwares have been used together: "Filter Design and Analysis" of Okawa [23] and "Webench Designer" [24] of Texas Instrument.

As shown in the figure 3.21, the Bessel typology has a -3 db cut-off frequency shifted compared to the other filters. So, in order to have the -3 db corner frequency at 3 MHz (obtained by the transfer function in the table 3.1), the FSF must be considered in the analysis (see subsection 3.4.2). In the Sallen-Key configuration the FSF is equal to 1.274.

The filter is therefore designed with a break frequency of 3 MHz $\cdot$ 1.274 $\simeq$ 3.8 MHz. The gain voltage to voltage is set instead at 4 for reasons concerning the board interface (see subsequent section 4.2.2).

The Bode diagram is the same shown in the figure 3.20.

In the electrical scheme of the figure 3.25 the values of resistances and capacitances are displayed.

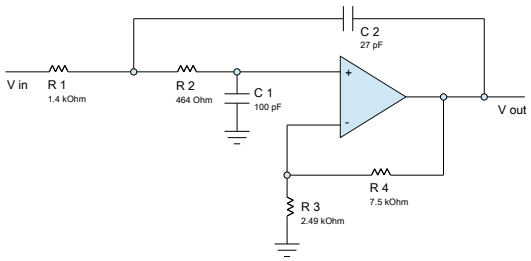

Figure 3.25: Second order low pass Bessel filter in the Sallen-Key configuration. Cut-off frequency is set at 3.8 MHz while the voltage to voltage gain is set at 4. Element values are shown.

Recapping, at this point the current sensor has been chosen - Sensitec CMS3050 - as well the proper analog filter - second-order low-pass Bessel in Sallen-Key architecture - to implement in the PCB. In the following chapter, the PCB design upgrade is explained.

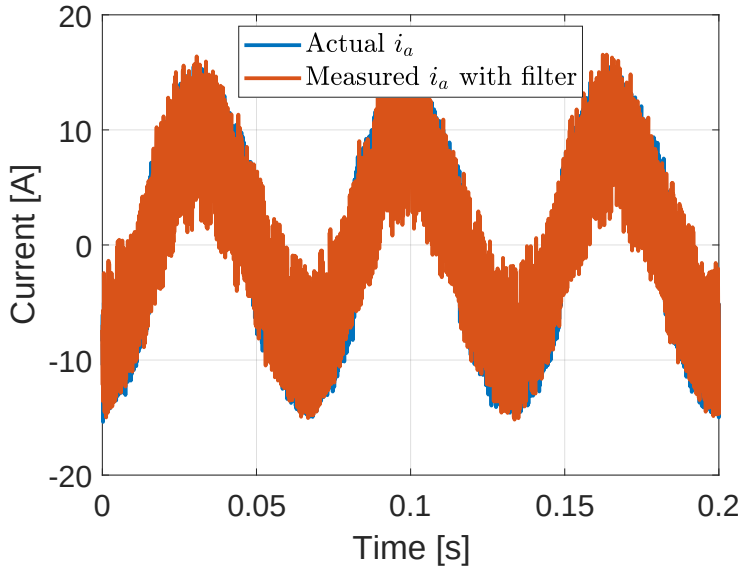

Figure 3.26: The designed Bessel filter (in orange) follows correctly the actual current (in blue). 0.2 s window.

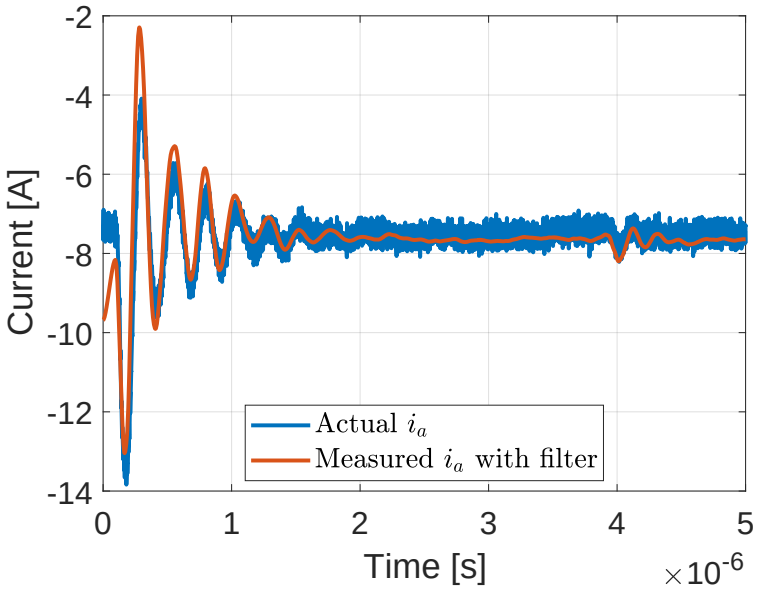

Figure 3.27: The deisgned Bessel filter (in orange) follows correctly the actual current (in blue). 5 us window. The rising at the beginning is due to a residual offset.

Chapter 4

PCB design upgrade

Once the device and the filter to implement are set, the PCB design is done starting from the previous measurement device design. The employed software is KiCad, a free software suite for electronic design automation. After a briefly view of the entire measurement system, the PCB design is explained step by step.

4.1 Introduction

The structure of the measurement system containing the PCB is shown in the figure:

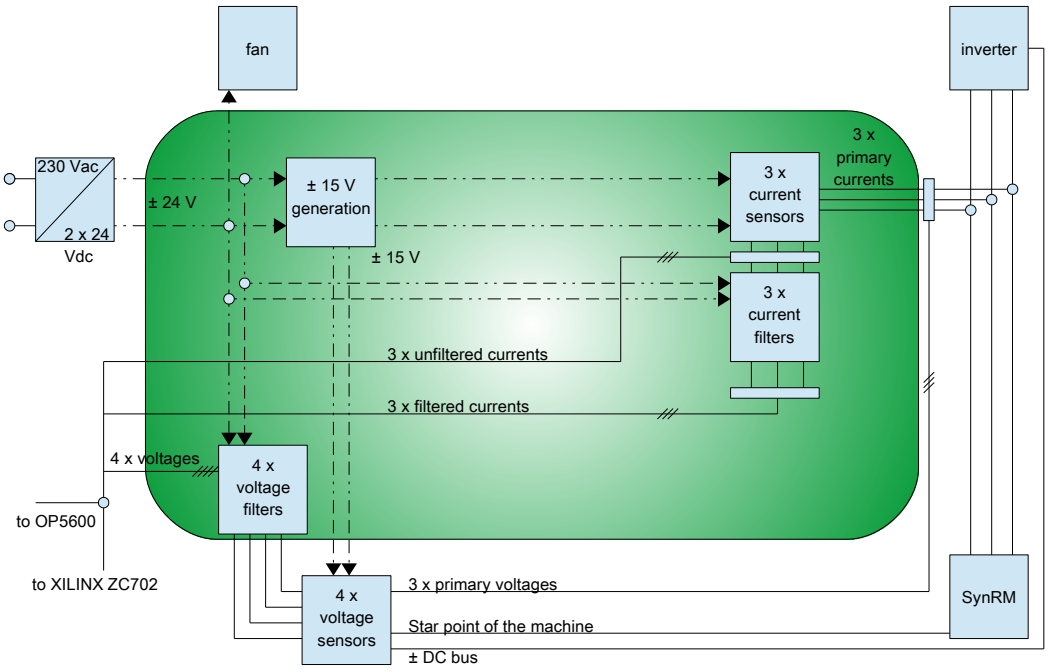

Figure 4.1: Schematic of the measurement system. The PCB is highlighted in green; arrows indicate the power supply line; solid lines indicate the signal

The power supply of the PCB is granted by two MeanWell MDR 60 ± 24 V_{DC} [25] which feed:

- The four analog filters of the voltage measurements, if present
- The three analog filters of the current measurements
- The cooling fan
- The power supply converters which transform ± 24 V_{DC} into ± 15 V_{DC}

That in turn feed:

- The three current sensors
- The four voltage sensors, if present

Primary currents and voltages come in from the three power cables located in the inverter-motor line. These enter in the three current sensors and - if devices are mounted - in the four voltage sensors.

At the output side ten signals are available: three filtered current signals, three unfiltered current signals and - if present - four voltages signals. The PCB has two typologies of output: one through DB7 connector, to interface with the analog input of an OPAL-RT OP5600 [26], and one through SMA connectors, to interface with FPGA XILINX ZC702 [27].

4.2 Structure of the PCB

The main part of the measurement system is the PCB, in which currents and possibly voltages are measured and filtered. The following section describes the board in details.

4.2.1 Power supply

The PCB is supplied by two MeanWell MDR-60-24 (24 V/ 2.5 A) [25] power supplies, connected in series to obtain a ± 24 V voltage source. For protection against over-voltages two Schottky diodes are mounted. The midpoint voltage of the two power supplies establishes the ground potential of the board. Figure 4.2 shows the schematic.

Current and voltage sensors require a power supply of ± 15 V. Additionally, the possibility to feed the fan with 15 V is included with a terminal block header. This stage (see figure 4.3) is realized by two LM2594HVM-ADJ [28] voltage regulators, supplied by the +24V line; one of them is designed to invert the voltage to -15V.

The first stage is made by the input capacitors, followed by a delayed start-up. Then the LM2594HVM-ADJ are mounted. At the output, a low-pass filter and one LED for each polarity is mounted to indicate whether the voltage is present or not.

The ± 15 V can supply a maximum current of 500 mA. The maximum current consumption within bounds for each Sensitec CMS3050 current sensor is 100 mA while each voltage sensor requires a maximum current of 32.2 mA in worst case operation. The total amount is so $3 \cdot 100$ mA $+ 4 \cdot 32.2$ mA $= 428.8$ mA and the limit of 500 mA is complied.

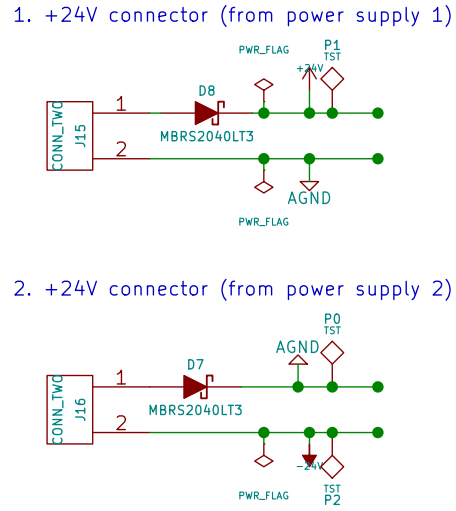

Figure 4.2: Schematic of power supplies ±24 V.

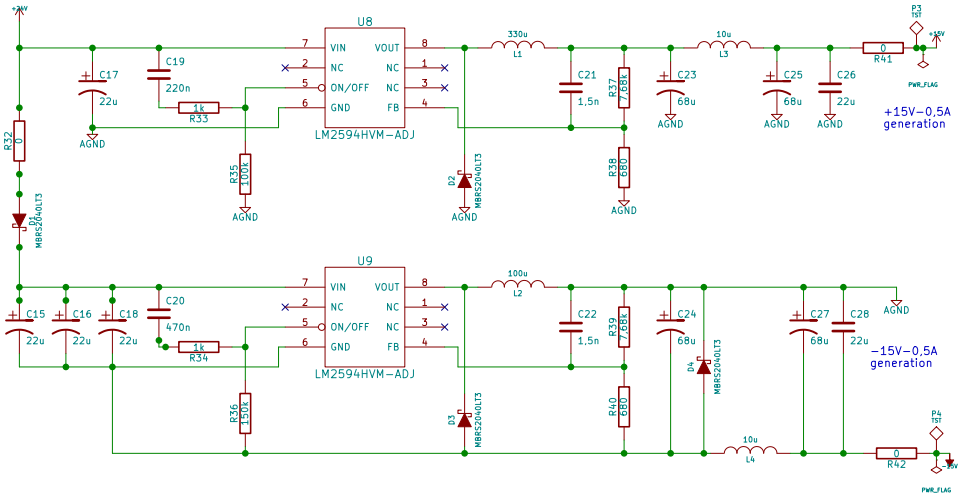

Figure 4.3: Schematic of the ±15 V regulation.

4.2.2 Current stage

The three current sensors Sensitec CMS3050 (look at chapter 2 for electrical data) are mounted in CMK boards (figure 2.4). These in turn are seated on the PCB through screws and the three unfiltered currents, by wires and terminal block headers, routed to the board.

Before the filtering stage, these unaltered signals are made available at the output stage.

In order to obtain an accurate measurement, the three 2^{nd}-order Bessel low-pass filter in Sallen-Key configuration - designed in the section 3.5 - have been arranged with a cut-off frequency of f_c= 3.8 MHz and a gain (voltage/voltage) of A = 4. The schematic of the filter is shown in the next image 4.4.

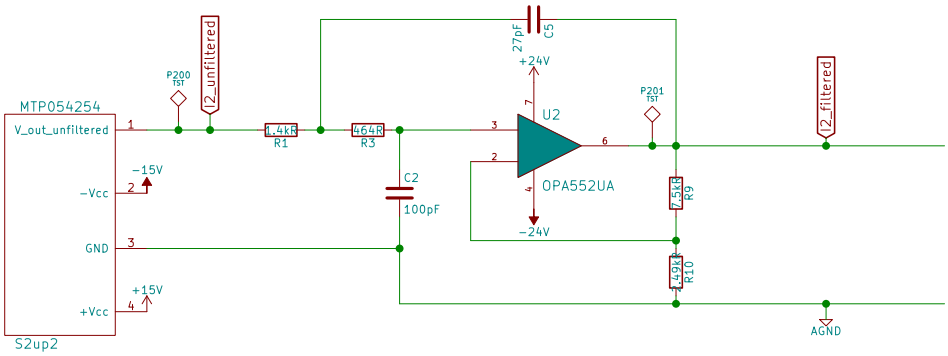

Figure 4.4: Current stage schematic: on the left, the current sensor that feeds the analog filter.

To match analog signals with the input of the OP5600, two factors were taken into account:

- The analog input of OP5600 has a voltage range of ±20 V.
- The op amp OPA552 [29] has a gain-bandwidth of 12 MHz. Considering that this parameter is the product of the op amp bandwidth - set for oversampling reason around 3 MHz - and the gain at which the bandwidth is measured, the best compromise concerns settling the gain at 4 V/V.

If the primary current is 50 Arms, the sensor output voltage is, according to the data sheet, 2.5 V. The peak value consequently is 2.5 V $\cdot\sqrt{2}$ = 3.535 V and so the signal available at the output is 3.535 V · 4 = 14.142 V.

Bypass capacitors are used to eliminate transient voltage peaks of the power supply which could affect the sensors. In the design one 10μF electrolytic capacitor and one 0.1 μF ceramic capacitor are mounted. Due to the different high-frequency characteristics, a ceramic and an electrolyte capacitor are needed to ensure a proper reduction of transient voltages of several types.

The output signals of the filters are connected to the PCB output.

4.2.3 Voltage stage

The measurement device, although is able to measure voltage, wasn't designed to test it. This means that, while in the PCB the filtering voltage stage is anyhow present, the voltage sensors aren't mounted within the system.

In the previous version four LEM CV 3-1500 sensors were used. The supply voltage of these device is ±15 V, equal to the one for current sensors. Four terminal block headers ±15 V are present in the PCB just in case. The voltage range is 0 - ±1500 V.

The filtering stage is made by four 2^{nd}-order Butterworth low-pass filter in Sallen-Key configuration, with a cut-off frequency of f_c= 200 kHz and a gain (voltage/voltage) of A = 2. The design is taken from the previous device. The schematic of the voltage filter is shown in the figure 4.5.

Voltage signals are available at the output in the same way as the current signals.

4.2.4 Output pins

The output pins are ten: three unfiltered current signals, three filtered current signals and - if present - four voltage signals. There are two connection possibilities, depending

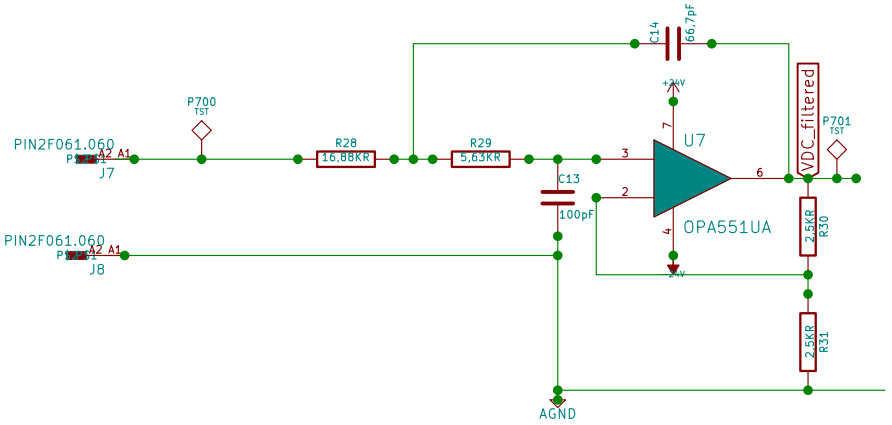

Figure 4.5: Voltage stage schematic: on the left the Faston connectors where voltage sensors can be connected.

on the used control device: with SMA connectors and with a DB37 connector. The schematic is resumed in the figure 4.6.

A shielded flat cable is assumed to connect the wire-to-board connector with 40 contacts to a DB37 plug at the case. For the XILINX ZC702 the same consideration for the gain (4 for current stage and 2 for voltage stage) is set but the possibility to connect the cable straight in the outside surface of the case is not covered.

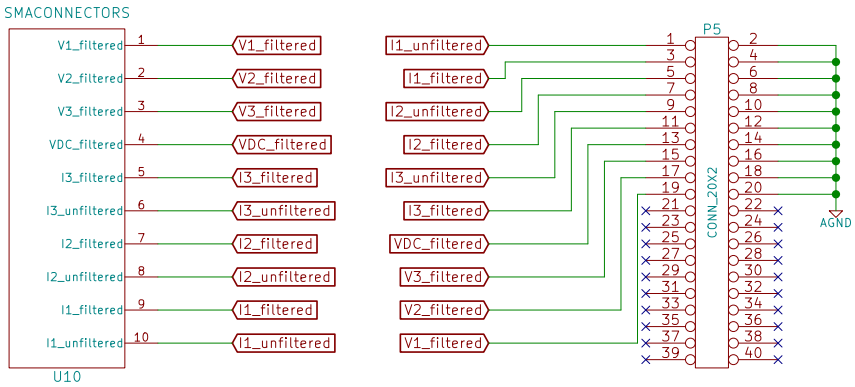

Figure 4.6: Left side: SMA connectors, right part: DB37 output.

4.3 PCB design

Figure 4.7 shows the top side of the PCB upgraded to the version 3.0. The bottom layer, where there are just the ±24 V traces, is shown in the image 4.8: as many wires as possible are routed on the top layer. The design is made using KiCad 4.0.7, stable release of 28 August 2017.

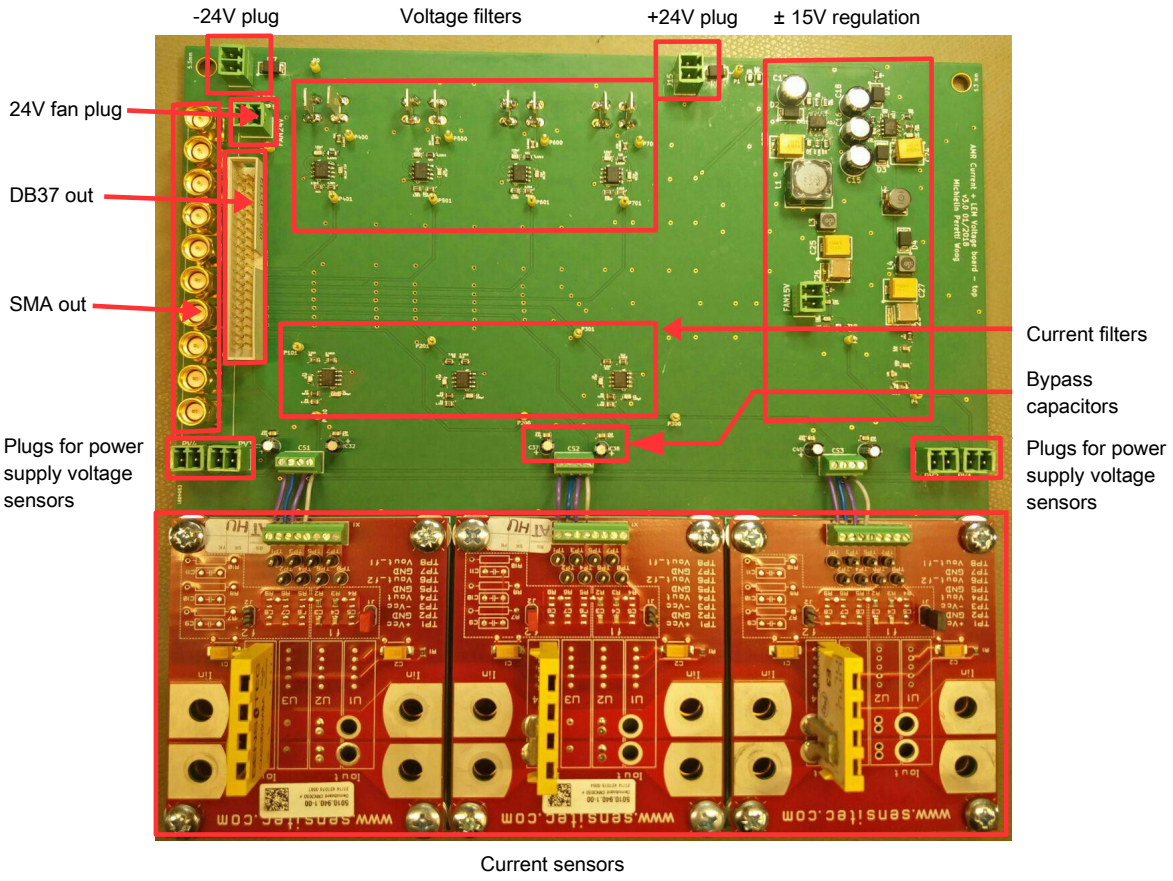

Figure 4.7: Top side of the PCB with description of the main area.

Copper traces have a width of 0.254 mm while the ±24 V power supply lines have a width of 0.508 mm. The board is grounded by the bottom copper layer and the vias between top and bottom layer ensure a optimal grounding. In certain spots of the board, test pins are mounted in order to detect signals and power supplies with an oscilloscope. The PCB is made of six layers. The top and bottom copper layers, connected each other by vias; here the wiring traces are routed. The top and bottom solder mask, which are overlaid onto the copper layers to insulate the traces from accidental contact with other metal. The top and bottom silk layer, with the component legends added in order to have an easier assembly. In this regard, in future board projects a positive symbol can be inserted in the power supply terminal blocks silk for the sake of clarity.

The dimensions of the new board are 230.5mm x 230mm, while the previous one were 174mm in length and 129.5mm in height. This is mainly due to accommodate the size of the current sensor evaluation boards.

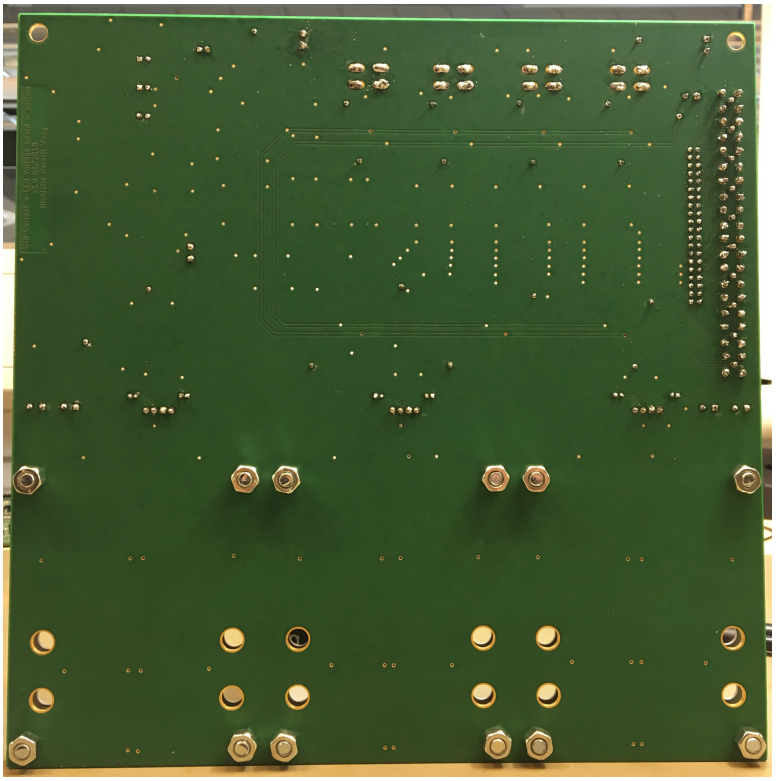

Figure 4.8: Bottom side of the PCB

Regarding the upgrades in this new PCB, the improvements concern:

- The magneto-resistive current sensors mounted in the CMK boards, visible on the bottom.
- The three analog filters of the currents.
- An added output, via SMA connectors.
- A new layout, due to the different geometrical disposition of the current sensors.

The general rules followed to design, with particular reference to high frequency behavior [30], are instead:

- To minimize the trace length
- A gap between traces of 0.2 mm
- To avoid right angles, preferring rather 45°
- A component tolerance (especially for capacitors) of 1%
- A capacitor range of [10pF, 10μF]
- A resistance range of [100Ω, 1MΩ]

Chapter 5

PCB testing

Once the PCB is designed and mounted, several tests were made in order to study its behavior.

5.1 Experimental outcomes: first motor

An induction motor, present at the bench, is connected to a converter.

Each phase of the converter is connected to the input side of the current sensor board while the output is connected to the machine. Figure 5.1 shows the set up under testing. Figure 5.2 show instead the line diagram of the set up.

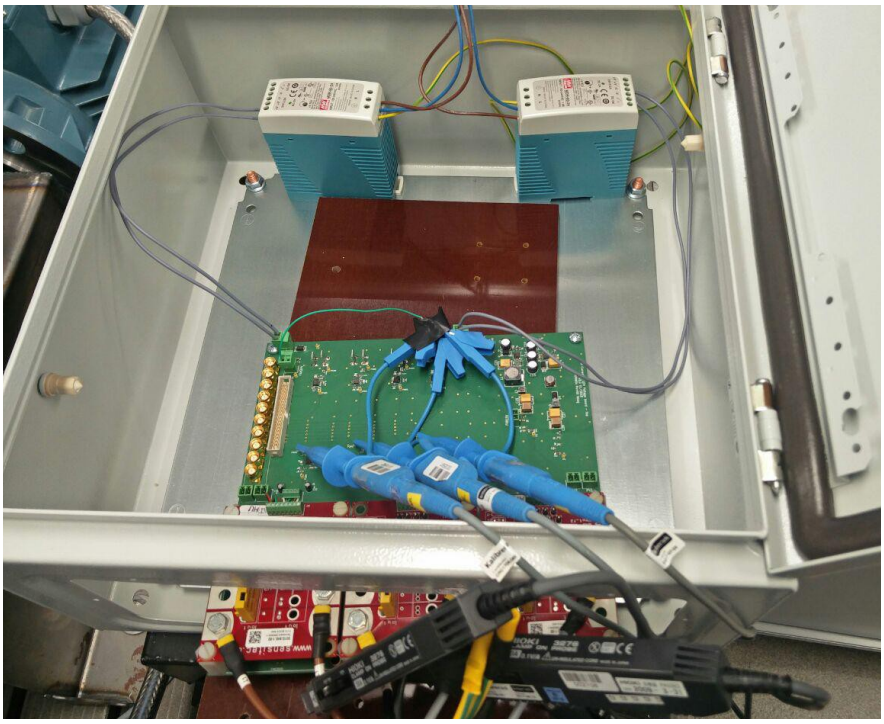

Figure 5.1: Set up for testing the board: power cables are visible on the bottom, PCB power supplies at the top.

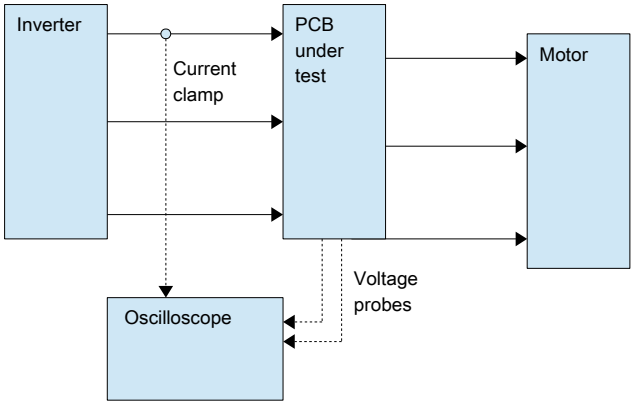

Figure 5.2: Line diagram of the set up. In solid-line the power cables, in dotted-line the measurements.

One current clamp (with bandwidth of 100 MHz [21]) and two voltage probes (with bandwidth of 100 MHz [31]) are connected to an oscilloscope: the current clamp measures the actual current in one of the phase (yellow trace in figure 5.3), one of the voltage probes is connected to the unfiltered current sensor output (green trace in figure 5.3) and the last voltage probe is connected to the filtered current sensor output on the designed PCB (magenta trace in figure 5.3).

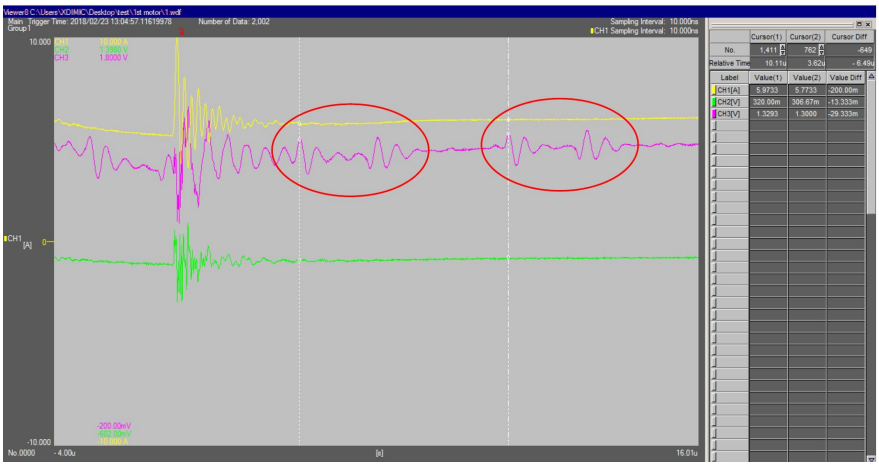

Figure 5.3: Current measurements for one phase. The difference in amplitude is due to the different current sensors gain; compensating this aspect, magnitudes are equivalent.

Two ripples repeating at 150 kHz, ringing at 2 MHz, are visible (marked by red circles) in the filtered current sensor output. The ripple phenomenon is due to the switching of the two step-down regulators present in the ±24 V to ±15 V voltage regulation (see section 4.3). The ringing frequency at 2 MHz is traced back instead to generic stray elements present in the op amp and the board surrounding it, which arise in the high frequency domain. Supplementary investigations (see figures 5.4 and 5.5) are performed in order to further assess this problem. Knowing that oscillations are due to a board problem - in particular to the switching of the two step-down regulators - only the PCB is fed for these last inspections.

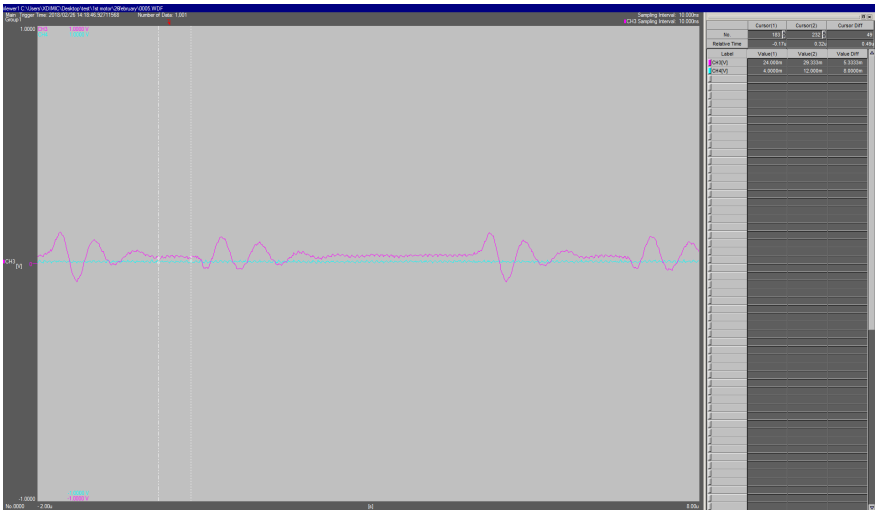

Figure 5.4: Probes connected to the unfiltered current test point (cerulean) and the filtered one (magenta). Note that there is no input. The problem is present just in the last case.

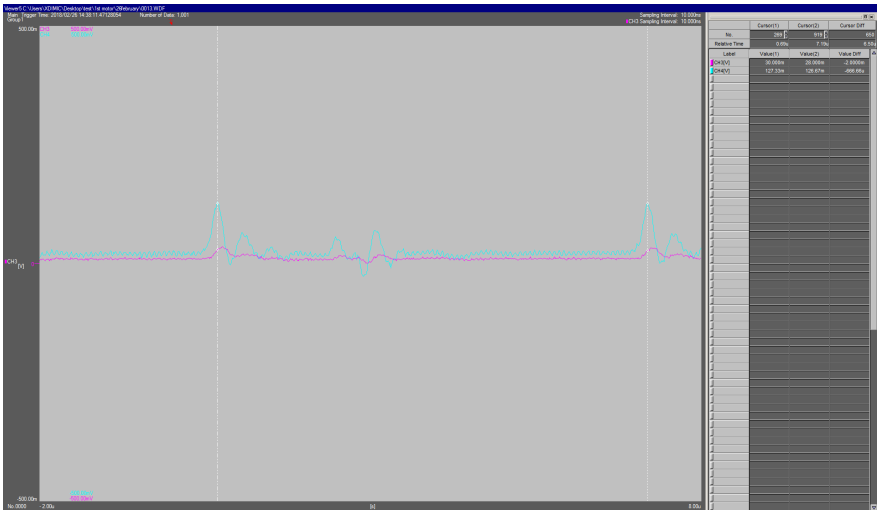

Figure 5.5: Probes connected to the unfiltered voltage test point (magenta) and the filtered one (cerulean). Note that there is no input. The problem is present in both cases, but in the unfiltered test point just the switching event is visible.

In order to assess thoroughly this effect, an identical PCB is connected. On this PCB only required components for phase 1 current filter are mounted (figure 5.6). From here on, PCB1 refers to the board comprehensive of all components, while PCB2 refers to this last experimental one.

More tests are carried out. The current signal - measured in the PCB1 - is transmitted to the PCB2 (i.e. white wire in the picture 5.6) but different arrangements for the ± 24 V power supplies are adopted. Firstly, both PCBs were fed by the two power supply devices MeanWell MDR-60-24. Then the boards are fed by four different MeanWell MDR-60-24 (two for each PCB). Lastly the four power supply equipments are connected, pairwise, just in the midpoint.

However, the result is similar to the previous set-up.

In order to solve the problem at source, the power supply required for ± 15 V is

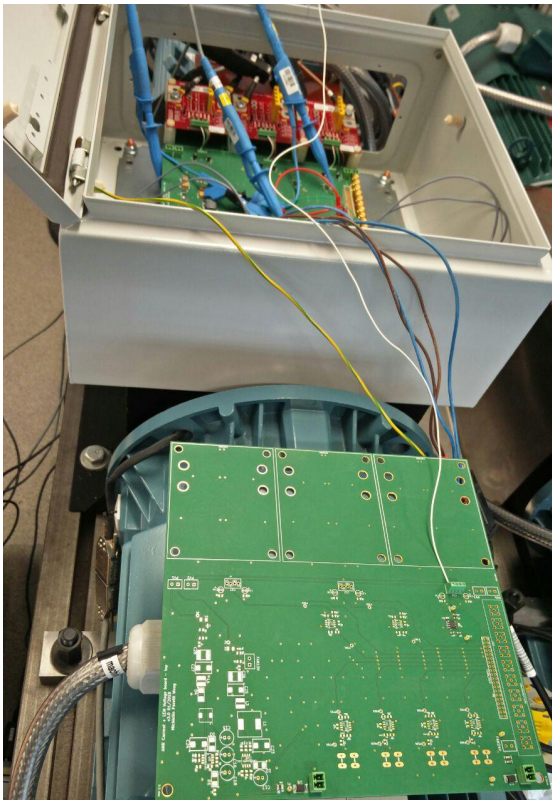

Figure 5.6: New set up. The second board insertion is done in order to evaluate different factors (ground influence, switching oscillations and op amps behavior).

replaced by two external DC generators. The aim of this test in fact is to eliminate the switching noise due to the two voltage regulators embedded in the PCB. The first PCB - where the current sensors were located - is fed just by this external source, while the second PCB - with the current filter - was fed by two MeanWell devices at ±24 V. The figure 5.7 reports the result.

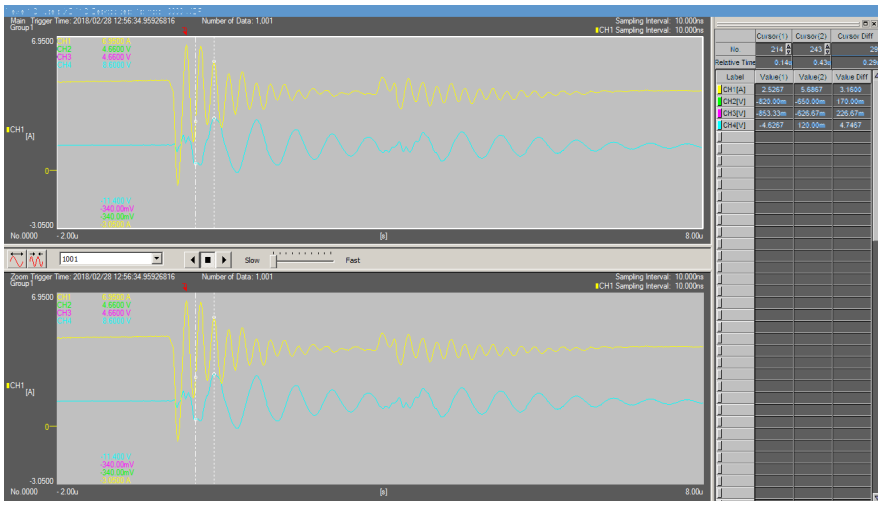

Figure 5.7: Probes connected to the actual current (yellow) and the PCB filtered current sensor output, in the second board (cerulean trace).

As it is possible to see, the switching noise disappears but anyway the signal is not yet properly followed. In fact, the actual current ringing has a frequency of 4.5 MHz circa, the filtered output has a ringing frequency equals to approximately 1.5 MHz. This fact has been interpreted as a poor dynamic of the current filtering op amps.

The purchase of new op amps, with improved performances, is therefore necessary. These two new devices manufactured by Texas Instruments - THS3061D [32] and THS3001CD [33] - show better performance in terms of slew rate (THS3061D, 7000V/μs), gain-bandwidth (THS3061D, 220 MHz) and 0.1% settling time (THS3061D, 30 ns). The power supply voltage required is lower ($\pm$15 V): a change in the feeding line is needed.

The THS3061D is mounted in the current phase 3 of the PCB2. The $\pm$15 V power supply is connected to both the boards: to power the current sensors in the PCB1 and the THS3061D - with the filtering stage - on the second board. The following pictures 5.8, 5.9, 5.10, 5.11 and 5.12 show the results. The main point to pay attention concerns the comparison between the actual current - yellow - and the filtered one - in magenta.

From here on, "PCB current" refers to the filtered current sensor output on the designed PCB with the THS3061D op amp.

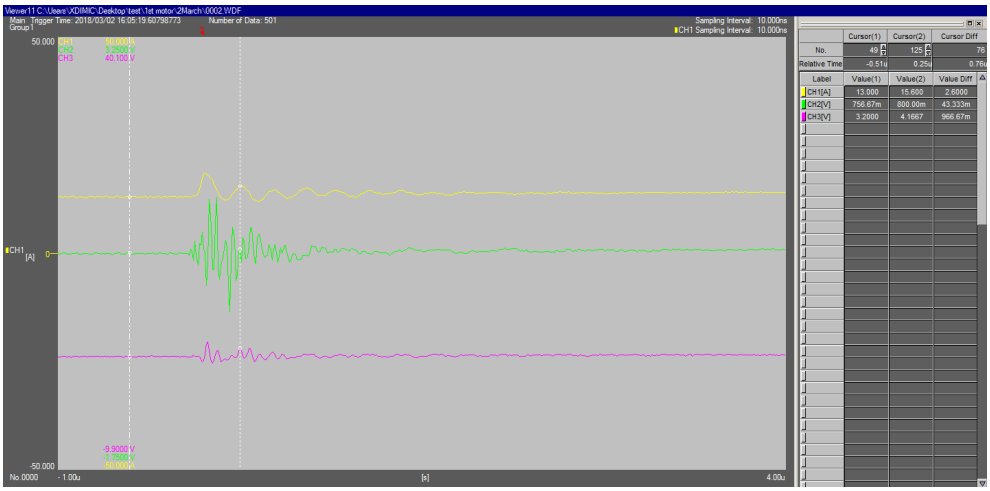

Figure 5.8: Actual current (yellow signal), PCB current (magenta signal) and unfiltered output from the current sensor (green signal).

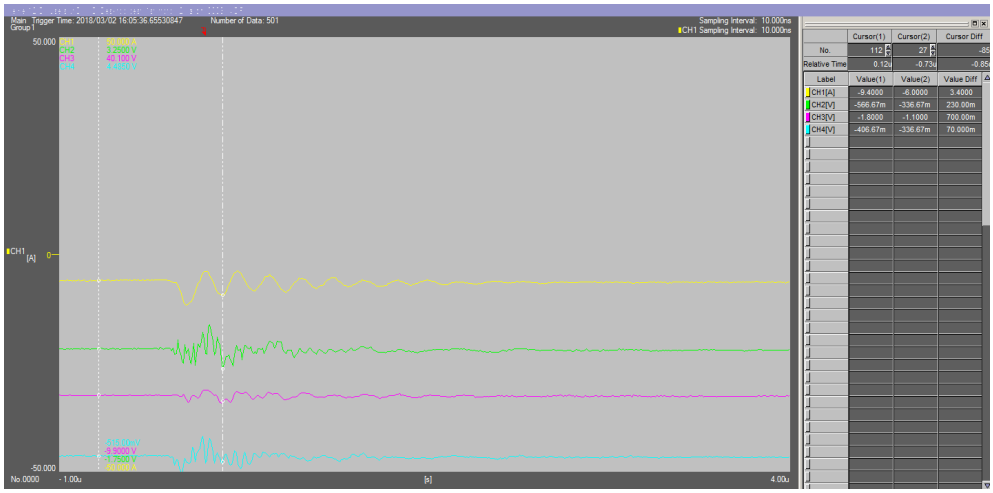

Figure 5.9: Actual current (yellow signal), PCB current (magenta signal), unfiltered output from the current sensor (green signal) and filtered - by the pre-assembled RC filter - output from the evaluation CMK board (cerulean signal).

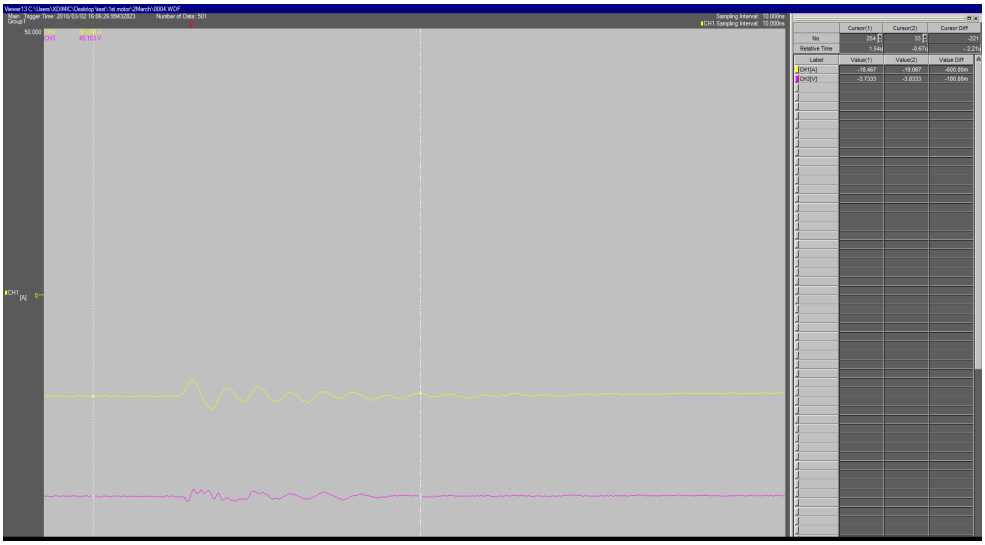

Figure 5.10: Actual current (yellow signal) and PCB current (magenta signal).

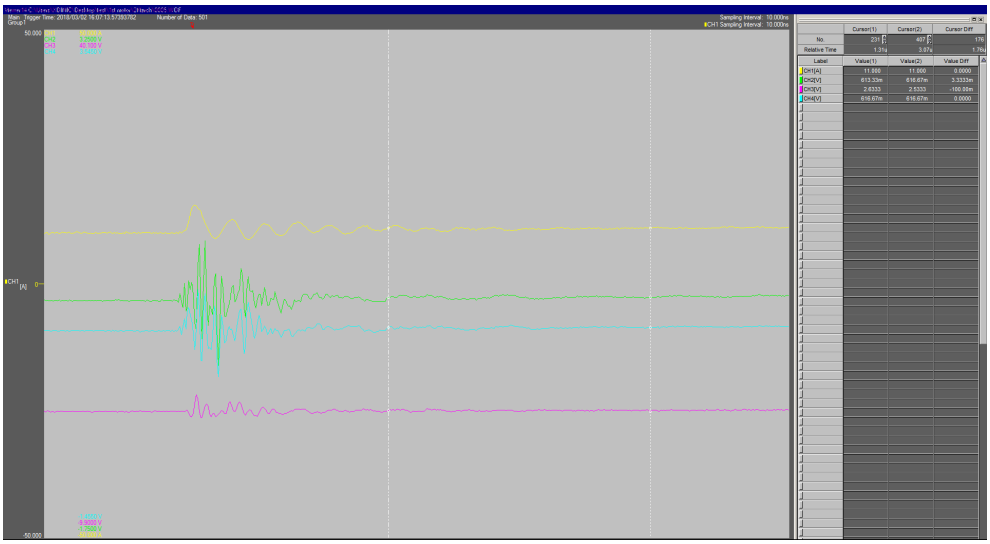

Figure 5.11: Actual current (yellow signal), PCB current (magenta signal), unfiltered output from the current sensor (green signal) and filtered - by the pre-assembled RC filter - output from the evaluation CMK board (cerulean signal).

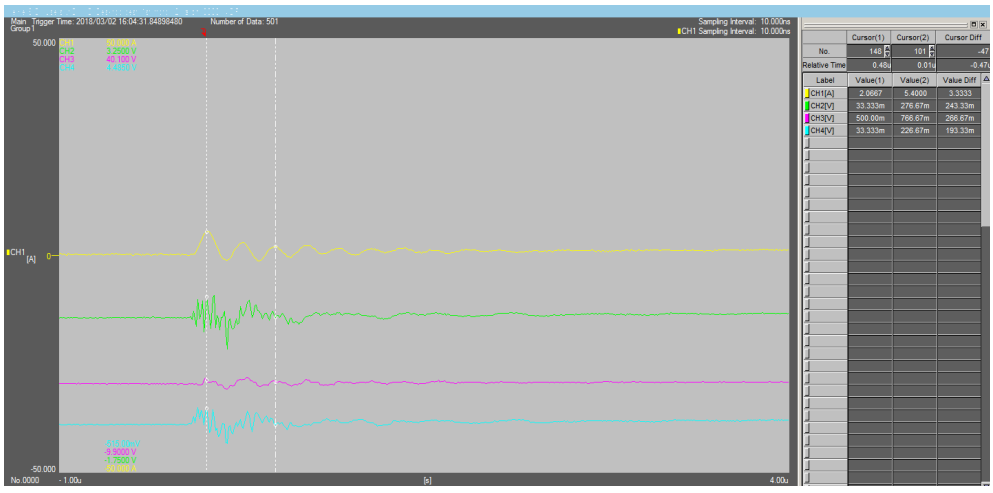

Figure 5.12: Actual current (yellow signal), PCB current (magenta signal), unfiltered output from the current sensor (green signal) and filtered - by the pre-assembled RC filter - output from the evaluation CMK board (cerulean signal).

With both a different power supply and an improved op amp, the results show a much improved behavior. Although some ripples are still present, the measurements taken using current sensors on PCB roughly follow the actual current. The cursors in previous images help this analysis.

This test is repeated at different speeds and had no effect on the measurements. This is due to the fact that the speed is related to the fundamental frequency while the device is tested in the high frequency domain (i.e. 4.5 MHz).

The measured data is than post-processed (i.e. compensation for gain and offset) using Matlab. The figures 5.13 and 5.14, shows comparison between actual current and current measured using newly developed PCB.

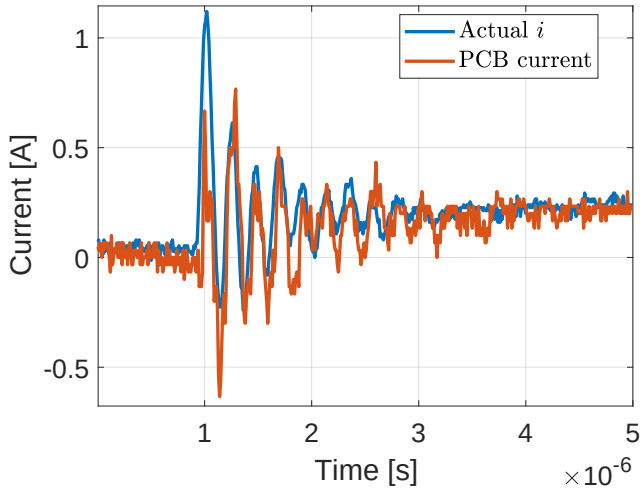

Figure 5.13: Actual current (blue) with the PCB current (orange).

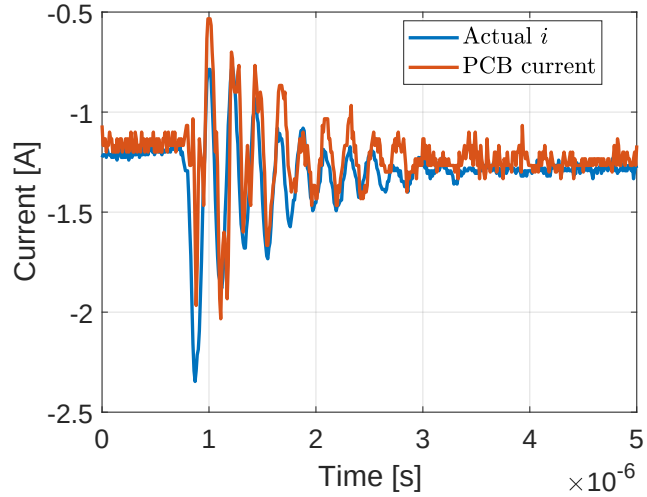

Figure 5.14: Actual current (blue) with the PCB current (orange).

Furthermore, a simulation is done in order to compare the PCB current with a current filtered using Matlab. In this way, the Bessel analog filter embedded in the PCB is evaluated in terms of correct cutoff frequency and poles.

Different digital IIR filters are designed with the Matlab command "*designfilt*" and are applied to the unfiltered output of the current sensor. All the filters used in this report are explained in the appendix B. The figures 5.15 and 5.16 show the outcomes:

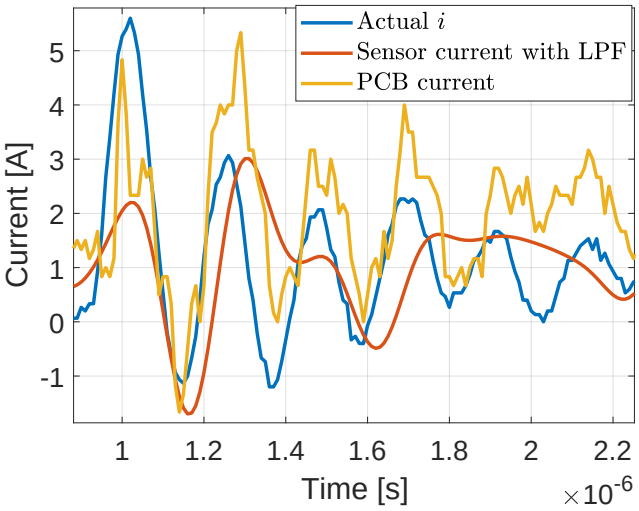

Figure 5.15: Comparison between the PCB current with a digitally filtered one. 4-th order Butterworth LPF with passband equals to 6.4 MHz.

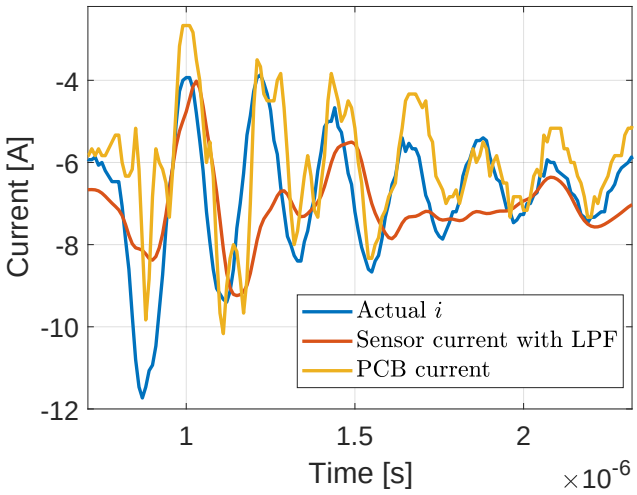

Figure 5.16: Comparison between the PCB current with a digitally filtered one. 2-nd order Butterworth LPF with passband equals to 8.6 MHz.

As it's possible to see in the figures (5.15 and 5.16), the current filtered using Matlab shows a smoother behavior. The current measured using the PCB contains more ripple but also more information regarding peak's magnitude and frequency.

A digital filter is applied even in the current measured using PCB. Results are reported in the figures below:

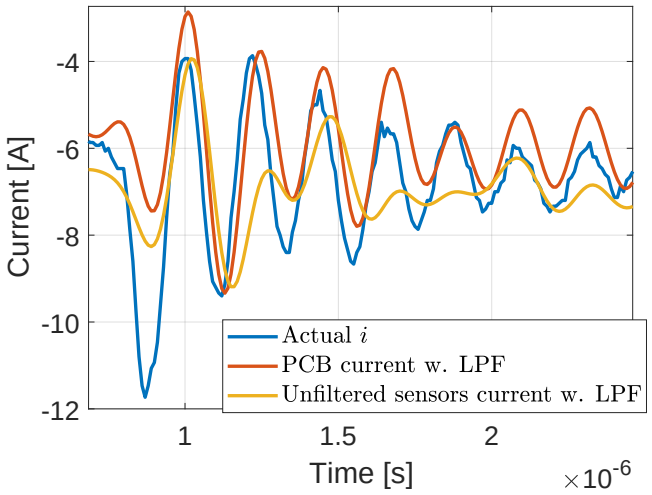

Figure 5.17: Comparison between the PCB current - beyond digitally filtered - with a digitally filtered one. 8-th order LPF with passband equals to 6 MHz.

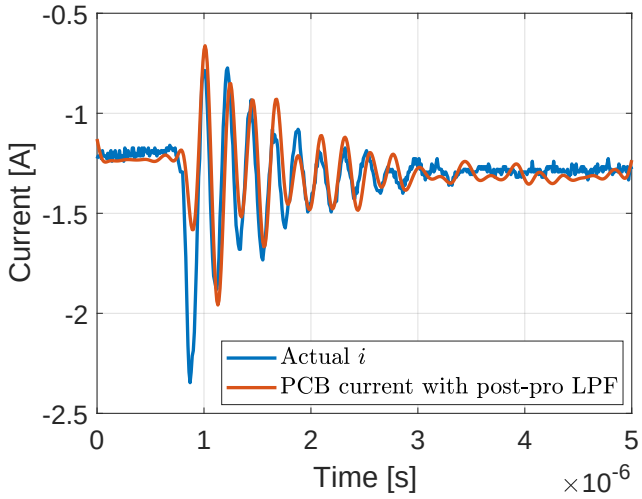

Figure 5.18: The PCB current - beyond digitally filtered. 4-th order LPF with passband equals to 6 MHz.

A digital filtering stage on the PCB current can improve the behavior in terms of smoothness.

5.2 Experimental outcomes: second motor

A second motor (synchronous reluctance machine), present at the bench, is connected to the converter.

The current and the speed range (200 rpm) used for these tests are similar to the the previous test performed in the section 5.1. The following figures 5.19, 5.20 and 5.21 show the measurements taken using the second motor.

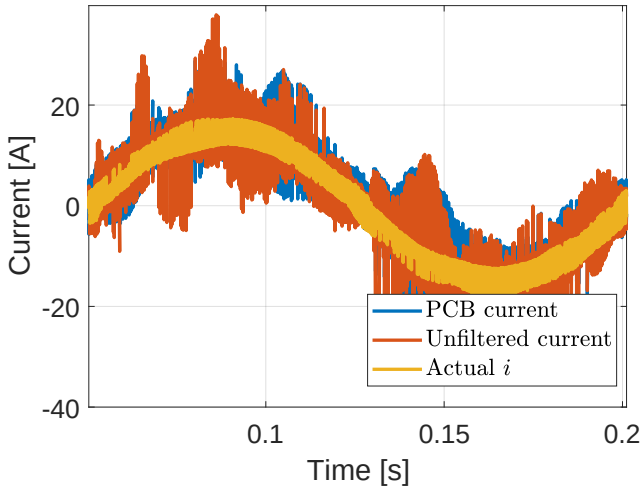

Figure 5.19: Actual current (yellow color), PCB current (blue color) and unfiltered output from the current sensor (orange color).

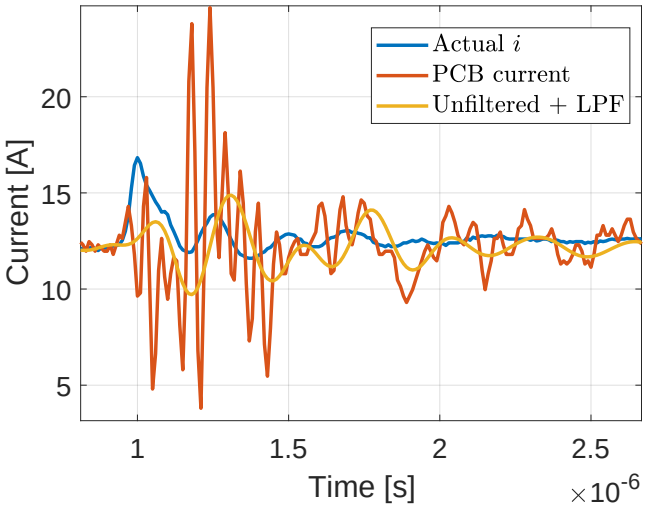

Figure 5.20: Actual current (blue color), PCB current (orange color) and a digitally filtered one (yellow color). 8-th order LPF with passband equals to 6.5 MHz.

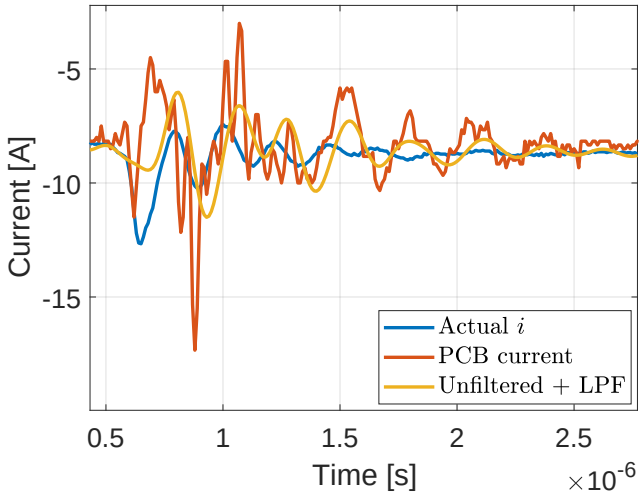

Figure 5.21: Actual current (blue color), PCB current (orange color) and a digitally filtered one (yellow color). 8-th order LPF with passband equals to 6.5 MHz.

The outcomes show that, even in this case, the PCB current has a better behavior in terms of frequency content in spite of its noisier performance. The first peak reveals itself as the most troublesome (compare the tests with the first motor 5.1). At the end of the ringing stage some information is missed and the current sensor starts to lose the actual signal. This phenomenon is traced back to a physical inherent limit of the measurement device, that has anyway a limited bandwidth; further investigations in this direction should be done.

5.3 Experimental outcomes: third motor

Similar tests are carried out on a third machine (Interior Permanent Motor).

The current and the speed range (200 rpm) used for these tests is similar to the previous tests. The figures 5.22, 5.23 and 5.24 provide to show the outcomes.

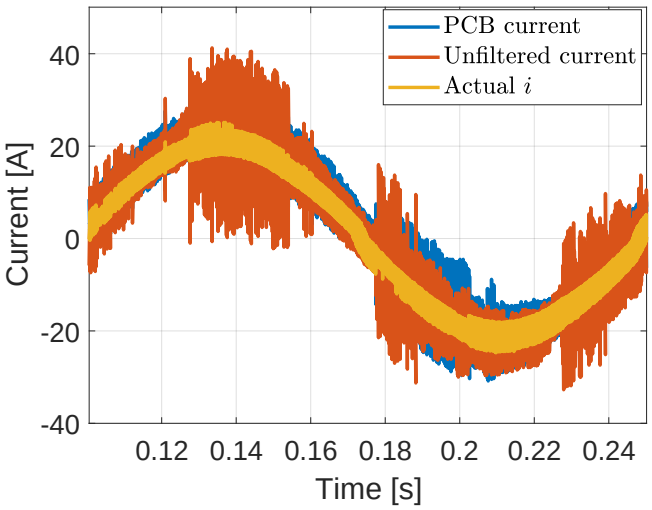

Figure 5.22: Actual current (yellow color), PCB current (blue color) and unfiltered output from the current sensor (orange color).

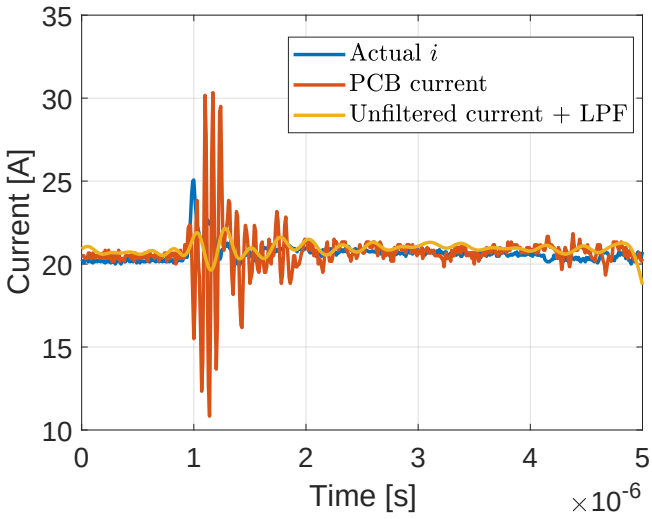

Figure 5.23: Actual current (blue color), PCB current (orange color) and a digitally filtered one (yellow color). 8-th order LPF with passband equals to 5.0 MHz.

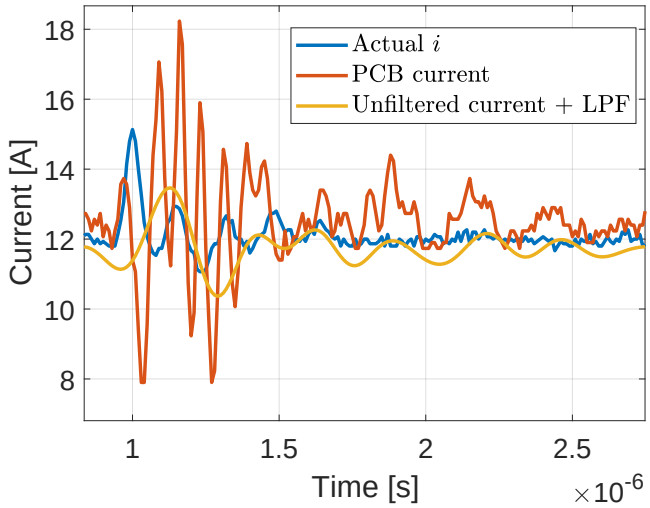

Figure 5.24: Actual current (blue color), PCB current (orange color) and a digitally filtered one (yellow color). 8-th order LPF with passband equals to 5.0 MHz.

In this case the actual current ringing has a frequency value equals to 6 MHz, more than the 4.5 MHz of previous investigations. *A fortiori* the device can not follow the signal properly, having a physical limitation in terms of bandwidth. Therefore, this last parameter should be in a range of 4.5 MHz - 6 MHz, since the signal can be reproduced with acceptable accuracy till 4.5 MHz.

5.4 Experimental outcomes: fourth motor

Last investigation is carried out on a Permanent Magnet Assisted Synchronous Reluctance Motor.

The current and the speed range (200 rpm) used for these tests is same as the previous tests. The following figures 5.25, 5.26, 5.27 show 5.28 the measured results.

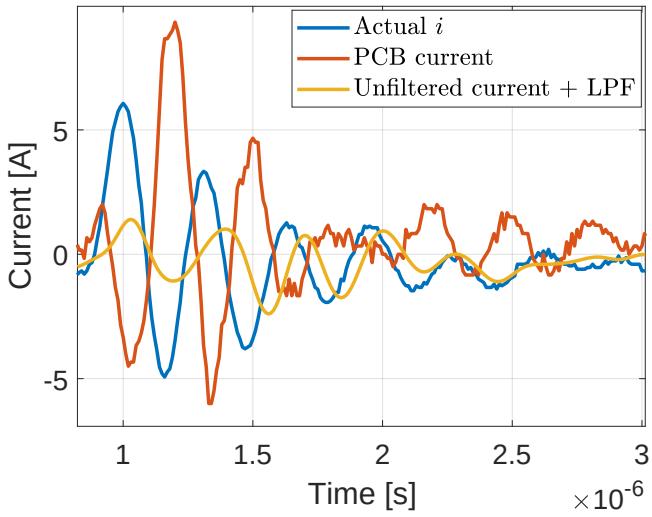

Figure 5.25: Actual current (yellow color), PCB current (blue color) and a digitally filtered one (yellow color). 6-th order LPF with passband equals to 6.7 MHz.

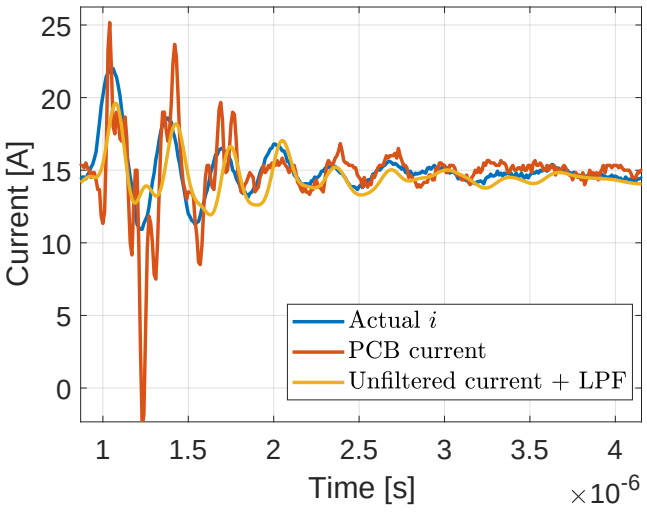

Figure 5.26: Actual current (blue color), inverted PCB current (orange color) and a digitally filtered one (yellow color). 6-th order LPF with passband equals to 6.7 MHz.

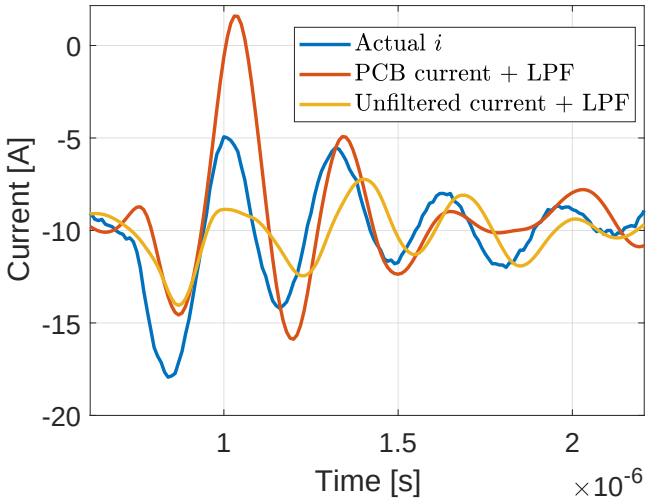

Figure 5.27: Actual current (blue color), inverted PCB current - beyond digitally filtered (orange color) and a digitally filtered one (yellow color). 2-nd order LPF with passband equals to 2.8 MHz.

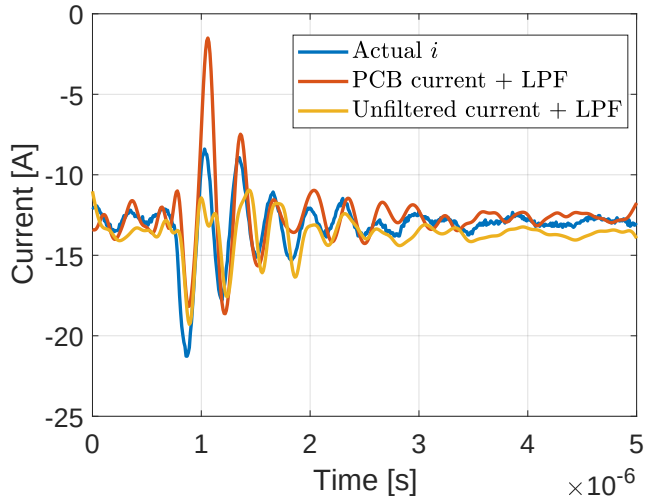

Figure 5.28: Actual current (blue color), inverted PCB current - beyond digitally filtered (orange color) and a digitally filtered one (yellow color). 8-th order LPF with passband equals to 7.2 MHz.

The actual current ringing has a frequency value equals to 3 MHz in this instance. The figure 5.25 show that the PCB current - during the oscillation - reverses although the frequency content is not lost. This problem happens after the current sensor, in the PCB stage; further investigations in this direction should be done.

In the subsequent simulations (figures 5.26, 5.27 and 5.28) the PCB current is inverted: the device - with the filtering stage - follows the signal properly.

5.5 Remarks on the results

After fixing several issues with the new design, such as ripple due to voltage regulator and slow dynamic of the op amp, several tests are carried out on four different type motors. The current sensors are mounted on PCB1 which is power by an external ± 15 V power supply. The conditioning stage is assembled on PCB2 which is also powered by the ± 15 V power supply. The output of PCB1 is fed to PCB2 via jumpers.

The measured quantities are: actual current, unfiltered output from the current sensor, filtered current - by pre-assembled RC filter - output from the evaluation CMK board, PCB current (in some case beyond digitally filtered) and the digitally filtered current from the unfiltered output.

The current in the first machine 5.1 is well-reproduced except the troublesome first peak. The addition of a digital filter offers the possibility to have a cleaner signal (figure 5.18).

In the second machine 5.2, in spite of the same harmonic content, the current sensor can roughly reproduce the signal (see figure 5.21). However the issue primarily manifested when the oscillations are ending. Further investigations to solve this problem are required.

The ringing frequency in the third machine investigated in section 5.3 is instead 6 MHz, which is higher than previous cases. This change in terms of frequency is due to the different high-frequency circuital models that each machine has. The signal does not follow the actual current (figure 5.24). That is due to the intrinsic limit in terms of bandwidth and the only way to solve it concerns an upgraded current sensor.

In the last machine, i.e. section 5.4, the actual current ringing has a frequency of 3 MHz. However, the PCB current results are reversed during the switching instants. This could be traced back to a problem in the designed board or in the set up; thus requires further investigation to solve this problem. Anyway once the current is inverted the actual current is reproduced correctly (figure 5.26).

The new current sensors and PCB design can detect - in magnitude and frequency - the switching instant with its subsequent oscillations. Some issues are highlighted in this report and are yet to be solved. The work has therefore shown that an hardware upgrade of drive measurement boards has good potential in an oversampling perspective.

Chapter 6

Conclusions

The work provides a design of a printed circuit board (PCB) for the measurements of phase currents in electrical machines, with the focus on a configuration that allows high-frequency sampling in the MHz range. This project is necessarily influenced by external factors: the research in the current technology area is focusing, *inter alia*, on high bandwidth and compact dimensions. The Sensitec CMS3050 provides the best trade off at the present time but new improvements cannot be ruled out in the future. The PCB can successfully measure the phase currents in the high-frequency domain. Also in the case of an upgrade hardware design, this method aids for the involved procedure and for the remarks made.

The first step focuses on evaluation of the current sensors available in the market. After this selection, the electronic design of the board and the conditioning stage (filtering and amplification) of the sensor output are finalized. The analysis demonstrate that an analog second order low-pass filter, with a cut-off frequency equals to 3 MHz, is suitable for the purpose. The Bessel typology is chosen for its suitable behavior in the time domain while the Sellen-Key topology is chosen thanks to the least dependence on the op amp performance.

Once the PCB is manufactured and assembled, several tests with different machine types are performed. These investigations show that the current high-frequency phenomena are replicated with different degree of precision as appropriate.

The switching oscillations have a frequency in a range of 3 - 6 MHz depending on the machine: this change in terms of frequency is due to the different high-frequency circuital models that each machine has. The current sensors can properly replicate the high-frequency phenomena till 4 - 4.5 MHz, which is likely the maximum physical bandwidth of the device. It is must be noted that the device declared range bandwidth is from DC to 2 MHz, when the output of the sensor is filtered with an on-board RC filter.

The first peak in the switching ringing is often barely followed, especially in terms of magnitude. The inversion problem observed in the last machine is due to an error in the set up and is not fixed because of time.

The work has shown that an hardware upgrade of drive measurements board with available solutions is possible and has a good potential for incorporating condition monitoring features in electric drives.

Regardless some aspects ought to be considered by possible future users:

- The reproduction of the current high-frequency behavior, in this work is analyzed in absolute terms, should be reasoned according to the used model i.e. in relative terms. This means that the informations carried by the current sensor may or may not be used in the ageing model or in the intrinsic PWM injection method. Further investigations ought to be done because this aspect isn't considered in this work.
- In the case of new advances in technology, the current sensor must have an output that can be easily embedded in a PCB. More-over the system requirements should be fulfill.
- The board conditioning stage ought to be designed according to the measuring device features. The filter cut-off frequency (in this work is set at 3 MHz) depends on the sensor's features; the gain (in this work: 4) must take into account instead the input range of the drive control unit.

Chapter 7

Future work

7.1 Improvement for voltage measurements

The device is meant for current measurements. However there's the possibility, with few adjustments, to detect voltages.

The set up consists mainly of three parts: the inverter, the measurement board and a motor. There are two power cables: from converter to board and from board to the machine. If the board functionality will be extended to measure even voltages, the star point of the machine should be available at the box as well.

Voltage sensors should be mounted inside the box by screwing. In the previous box, the chosen devices were the LEM CV 3-1500 but it is possible to use different sensors with improved features. The new box is meant to be enough large to install these devices likewise.

The voltage filtering stage is already present in the PCB (see 4.2). The voltages, from the sensors, can be connected to the board by Faston terminals. The second order Butterworth LPFs have a cut-off frequency of 200 kHz and a gain equal to 2. In the case of a power supplies improvement (see next section 7.2), the voltage stage op amps have to be improved in order to fulfill the new voltage requirements ($\pm$ 15 V).

7.2 Power supplies improvement

The PCB was initially designed with the op amp OPA552 in the current stage. However, due to the poor performances of this OPA552, the THS3061D is used as replacement. All the tests are performed using this new op amp.
OPA552 and THS3061D require different power supplies, one $\pm$ 24 V and the other one $\pm$ 15 V. Furthermore the - hypothetical - voltage conditioning stage requires $\pm$ 24 V while the current sensors $\pm$ 15 V.
If other tests should be carried (without voltage measurements), the PCB can be powered only by two power supplies at $\pm$ 15 V, taking care to disconnect the voltage regulators line, source of noise.
That could be done by making an open circuit. The easiest way is the removal of a board component upstream and downstream of the voltage regulators.

In future, this stage can be redesigned according to the new requirements for sensors and op amps. If the devices used will remain the same, the voltage regulators are not needed, since the only power supply required is $\pm$ 15 V.

7.3 Tests with the THS3001CD

Another op amp (THS3001CD [33]) is also purchased but it wasn't tested. Its features are similar to THS3061D [32]: slew rate of 6300V/μs, settling time (0.1 %) of 40 ns and gain-bandwidth equals to 350 MHz. Since both are extremely well-performing in terms of dynamic proprieties the results shouldn't be different. Further investigation could be done anyway for the sake of completeness.

It must be noted that the PCB1 is complete of all components while the PCB2 has only two current conditioning stages: one in the phase 1 (with OPA552) and one in the phase 2 (with THS3061D). In case of future use, the PCB1 should be upgraded by replacing the OPA552 with new op amps.
More-over, in the case of a re-design of the conditioning current stage, the filter gain can be set to higher values since the limit in the gain-bandwidth (see section 4.2.2) should no longer be accomplished.

7.4 Box

Since the task required more effort in testing the PCB, the box wasn't assembled. The additional material, which is already purchased, is:

- The alluminium case. The dimensions are 400 x 400 x 200 mm
- For the power supply two MeanWell MDR-60-24 V voltage sources are used. Due to the project changes, these devices should probably be replaced in future works.
- The power entry module, in order to connect the power supplies with the 230 Vac grid. A fuse holder is included [34].
- An axial fan, designed for 24 V [35].
- The input and output of both currents and voltages was thought connectors manufactured by "Phoenix Contact" [36].

Appendix A

Appendix A

This appendix provides the list of different TFs used in the frequency analysis (see 3). In the body of the report only the last four filters are compared in terms of RMSD. At the end a Bessel filter in a Sallen-Key configuration - marked with a star - was chosen.

```
% the RC two-poles filter already in place in the board
numRC = [490065394326.22];
denRC = [1 8823921.4640802 490065394326.22];
G_RC = tf (numRC,denRC);
```

```
% 1       sysidn tf 2-pole for TARGET (3MHz)
num1 = 5.086e14;
den1 = [1 3.606e7 4.794e14];
G1 = tf(num1,den1);

% 2      RC cascade two-poles to implement  (1.25 MHz)
num2 = 6.25e14;
den2 = [1 87500000 6.25e14];
G2 = tf(num2,den2);

% 3       short_5, 3 poles 1 zero (3 MHz)
num3 = [1.039222992325427e+15 1.120683192130224e+22];
den3 = [1 1.13918e+08 1.1976706e+15 1.10376483e+22];
G3 = tf(num3,den3);

% 4       short, 2 poles
num4 = 5.085745506253996e+14;
den4 = [1 3.6055679e+07 4.79426367e+14];
G4 = tf(num4,den4);

% 5       short_4, 3 poles 1 zero
num5 = [6.593767228138800e+14 1.724896629436997e+21];
den5 = [1 5.557371e+07 6.2179524e+14 1.696130e+21];
G5 = tf(num5,den5);
```

```
% 6      Bessel 2-nd order, MFB configuration
num6 = 3.6075036075036e15;
den6 = [1 43963150.670468 6.5990919649456e14];
G6 = tf(num6,den6);

% 7      Butterworth 2-nd order, MFB configuration
num7 = 2.2878059940517e15;
den7 = [1 28507696.833023 4.0853678465209e14];
G7 = tf(num7,den7);

% RMSD(long...short8) = [13.98 13.15 17.01 13.98...
... 12.81 16.08 12.94]
```

```
%    Bessel MFB (with minus sign)
num81 = 3.7515388812491e15;
den81 = [1 53058585.619475 9.3248126924874e14];

%    Butterworth MFB (w. minus sign)
num9 = 1.4682778569016e15;
den9 = [1 27327687.170532 3.6525677551319e14];

%    Bessel SK
num101 = 1.4095909329016e15;
den101 = [1 26593858.966829 3.5133948177426e14];

%    Butterworth SK
num11 = 1.4095909329016e15;
den11 = [1 26593858.966829 3.5133948177426e14];

% RMSD (long...short8) = [19.84 11.82 11.78 11.78]
% RMSD (m1...m12) =      [NaN 10.53 10.16 10.16]
```

```
% 8    Bessel MFB (w. minus sign)
num8 = 1.412728685456e15;
den8 = [1 33292197.99808 3.6010731197897e14];

% 10*    Bessel SK
num10 = 2.2874750232457e15;
den10 = [1 41361395.225126 5.701514322204e14];

% RMSD (long...m12) = [10.53 11.15 11.78 10.93]
% digitally (long...m12) = [12.29 12.03 12.48 12.03]
% noisy (long...m12) = [36.73 37.33 37.49 37.30]
```

Appendix B

Appendix B

This appendix provides the list with the features of different digital filters used in the PCB testing analysis (see 5). In the core of the report only some outcomes are shown.

```
% First motor, IM

1) LPF, 2nd order, f_cutoff= 3 MHz,      passbandripple= 0.1
2) LPF, 4th order, f_cutoff= 3 MHz,      passbandripple= 0.1
3) LPF, 4th order, f_cutoff= 5 MHz,      passbandripple= 0.1
4) LPF, 2nd order, f_cutoff= 10 MHz,     passbandripple= 0.1
5) LPF, 8th order, f_cutoff= 4.5 MHz,    passbandripple= 0.1
6) LPF, 8th order, f_cutoff= 3 MHz,      passbandripple= 0.1
7) LPF, 8th order, f_cutoff= 10 MHz,     passbandripple= 0.1
8) LPF, 2nd order, f_cutoff= 5 MHz,      passbandripple= 0.1

Butterworth filters (LPF)
9) half-power_frequency= 4 MHz
10) half-power_frequency= 6 MHz
11) half-power_frequency= 4.5 MHz, 2nd order
12) half-power_frequency= 4.8 MHz, 6th order

PCB+LPF w unfiltered+LPF
13) half-power_frequency= 5 MHz, 2nd order
14) half-power_frequency= 6 MHz, 6th order
15) half-power_frequency= 4 MHz, 4th order
16) butterworth, half-power_frequency= 4.8 MHz, 2nd order
17) butterworth, half-power_frequency= 6.4 MHz, 4th order
18) butterworth, half-power_frequency= 8.6 MHz, 2nd order
19) passband= 9.2 MHz, 4-th order

20) passband= 6 MHz, 8-th order
21) passband= 7 MHz, 2-nd order
22) passband= 4.5 MHz, 4-th order
```

% Second motor, SynRM

1) LPF, 8th order, f_cutoff= 5 MHz
2) LPF, 8th order, f_cutoff= 6.5 MHz
3) LPF, 8th order, f_cutoff= 4.8 MHz
4) LPF, 4th order, f_cutoff= 5.8 MHz

% Third motor, IPM

1) LPF, 8th order, f_cutoff= 5 MHz
2) LPF, 4th order, f_cutoff= 3.5 MHz

% Foruth motor, PMASynRM

1) LPF, 6th order, f_cutoff= 6.7 MHz
2) LPF, 2nd order, f_cutoff= 2.8 MHz
3) LPF, 8th order, f_cutoff= 7.2 MHz

References

[1] J. Bjorngreen, A. Reinap, and Z. Huang, "PMSM diagnostic and prognostic."

[2] C. Zoeller, M. A. Vogelsberger, R. Fasching, W. Grubelnik, and T. M. Wolbank, "Evaluation and current-response-based identification of insulation degradation for high utilized electrical machines in railway application," *IEEE Trans. Ind. Appl.*, vol. 53, no. 3, pp. 2679–2689, 2017. [Online]. Available: https://doi.org/10.1109/TIA.2017.2661718

[3] A. Faggion and S. Bolognani, "A new proposal of rotor position estimation in IPM motor drives based on PWM current harmonics," in *2010 First Symposium on Sensorless Control for Electrical Drives (SLED)*, Padova, Italy, Aug. 9-10 2010, pp. 1–7. [Online]. Available: https://doi.org/10.1109/SLED.2010.5542797

[4] A. Faggion, S. Bolognani, and L. Sgarbossa, "Rotor position estimation in IPM motor drives based on PWM current harmonics," in *2011 IEEE International Electrical Machines and Drives Conferance (IEMDC)*, Niagara Falls, Canada, May 15-18 2011, pp. 430–435. [Online]. Available: https://doi.org/10.1109/IEMDC.2011.5994633

[5] R. Slatter, M. Brusius, and H. Knoll, "Development of high bandwidth current sensors based on the magnetoresistive effect," in *2016 18th European Conference on Power Electronics and Applications (EPE'16 ECCE Europe)*, Karlsruhe, Germany, Sep. 5-9 2016, pp. 1–10. [Online]. Available: https://doi.org/10.1109/EPE.2016.7695648

[6] C. Zoeller, M. Vogelsberger, J. Bellingen, P. Nussbaumer, and T. Wolbank, "Investigation of sampling frequency and jitter effects on transient current signal evaluation for insulation condition monitoring," in *2015 17th European Conference on Power Electronics and Applications (EPE'15 ECCE Europe)*, Geneve, Switzerland, Sep. 8-10 2015, pp. 1–9. [Online]. Available: https://doi.org/10.1109/EPE.2015.7309193

[7] P. Nussbaumer, T. Wolbank, and M. Vogelsberger, "Sensitivity analysis of insulation state indicator in dependence of sampling rate and bit resolution to define hardware requirements," in *2013 IEEE International Conference on Industrial Technology (ICIT)*, Cape Town, South Africa, Feb. 8-10 2013, pp. 1–6. [Online]. Available: https://doi.org/10.1109/ICIT.2013.6505704

[8] AllegroMicroSystem, "ACS730, 1 MHz bandwidth, galvanically isolated current sensor IC in small footprint SOIC8 package." [Online]. Available: http://pdf1.alldatasheet.com/datasheet-pdf/view/848428/ALLEGRO/ACS730.html

[9] C. Gudel, "Taking transducer technology to the limits of current measurement accuracy," May 2008. [Online]. Available: http://www.powerguru.org/taking-transducer-technology-to-the-limits-of-current-measurement-accuracy/

[10] J. N. Fritz, C. Neeb, and W. D. Doncker, "A PCB integrated differential Rogowski coil for non-intrusive current measurement featuring high bandwidth and dv/dt immunity," pp. 1–6. [Online]. Available: https://eldorado.tu-dortmund.de/bitstream/2003/33955/1/S05.2.pdf

[11] KeysightTechnology, "What is a Rogowski coil current probe?" [Online]. Available: https://community.keysight.com/community/keysight-blogs/oscilloscopes/blog/2017/11/29/what-is-a-rogowski-coil-current-probe

[12] N. Troster, J. Wolfle, J. Ruthardt, and J. Roth-Stielow, "High bandwidth current sensor with a low insertion inductance based on the HOKA principle," in *2017 19th European Conference on Power Electronics and Applications (EPE'17 ECCE Europe)*, Warsaw, Poland, Sep. 11-14 2017, pp. 1–9. [Online]. Available: https://doi.org/10.23919/EPE17ECCEEurope.2017.8099003

[13] S. Ziegler, R. C. Woodward, H. H. Iu, and L. J. Borle, "Current sensing techniques: a review," *IEEE Sensors J.*, vol. 9, pp. 354 – 376, 2009. [Online]. Available: https://doi.org/10.1109/JSEN.2009.2013914

[14] AnalogDevice, "Op Amp Common-Mode Rejection Ratio (CMRR)." [Online]. Available: http://www.analog.com/media/en/training-seminars/tutorials/MT-042.pdf

[15] N. Alexander, N. Nain, and W. Navaeeth-Kumar, "Shunt based, 200-A peak current measurement reference design using reinforced isolation amplifier," pp. 1–27. [Online]. Available: http://www.ti.com/tool/TIDA-00445

[16] TexasInstrument, "OPAx376 low-noise, low quiescent current, precision operational amplifier e-trim series, data sheet." [Online]. Available: http://www.ti.com/lit/ds/symlink/opa2376.pdf

[17] ——, "AMC 1220/B fully-differential isolation amplifier, data sheet." [Online]. Available: http://www.ti.com/lit/ds/symlink/amc1200.pdf

[18] SensitecSolutions, "CMS3050 data sheet." [Online]. Available: https://www.sensitec.com/fileadmin/sensitec/Service_and_Support/Downloads/Data_Sheets/CMS3000/SENSITEC_CMS3050_DSE_05.pdf

[19] ——, "CMK3000 data sheet." [Online]. Available: http://docs-europe.electrocomponents.com/webdocs/1275/0900766b812751bc.pdf

[20] Agilent, "33120A user guide." [Online]. Available: https://www.keysight.com/upload/cmc_upload/All/6C0633120A_USERSGUIDE_ENGLISH.pdf

[21] Hioki, "Clamp on probe 3276." [Online]. Available: https://www.hioki.com/en/products/detail/?product_key=5783

[22] AnalogDevices, "Basic Linear Design, Chapter 8." [Online]. Available: http://www.analog.com/media/en/training-seminars/design-handbooks/Basic-Linear-Design/Chapter8.pdf

[23] Okawa, "2nd order CR Low-pass filter design tool." [Online]. Available: http://sim.okawa-denshi.jp/en/CRCRkeisan.htm

[24] TexasInstrument, "WEBENCH Design Center." [Online]. Available: http://www.ti.com/design-tools/overview.html

[25] MeanWell, "MDR-60-24 - 60 W 24 V miniature din rail power supply." [Online]. Available: https://www.meanwelldirect.co.uk/product/60W-24V-2-5A-Miniture-DIN-Rail-Power-Supply/MDR-60-24/default.htm

[26] OPAL-RT, "OP5600 V2 user manual." [Online]. Available: https://www.opal-rt.com/wp-content/themes/enfold-opal/pdf/L00161_0335.pdf

[27] XILINX, "ZC702 evaluation board for the Zynq-7000 XC7Z020 all programmable SoC." [Online]. Available: https://www.xilinx.com/support/documentation/boards_and_kits/zc702_zvik/ug850-zc702-eval-bd.pdf

[28] TexasInstrument, "LM2594 simple switcher power converter 150-kHz 0.5A step-down voltage regulator." [Online]. Available: http://www.ti.com/lit/ds/symlink/lm2594.pdf

[29] ——, "OPA55x high-voltage, high-current operational amplifiers." [Online]. Available: http://www.ti.com/lit/ds/sbos100b/sbos100b.pdf

[30] ——, "PCB design guidelines for reduced EMI." [Online]. Available: http://www.ti.com/lit/an/szza009/szza009.pdf

[31] Yokogawa, "700929 Isolated passive probe 100V / 100MHz." [Online]. Available: https://tmi.yokogawa.com/ca/solutions/products/oscilloscopes/voltage-probes/700929-101-probe/

[32] TexasInstrument, "THS3061 low-distortion, high slew rate, current-feedback amplifiers." [Online]. Available: http://www.ti.com/lit/ds/symlink/ths3061.pdf

[33] ——, "THS3001 420 MHz high-speed current-feedback amplifier." [Online]. Available: http://www.ti.com/lit/ds/symlink/ths3001.pdf

[34] KEC, "IEC Appliance Inlet C14 with fuseholder 1- or 2- pole and voltage selector." [Online]. Available: http://www.farnell.com/datasheets/1719090.pdf

[35] W2G107-AD03-01, "EC axial compact fan." [Online]. Available: https://eu.mouser.com/ds/2/120/ebm-papst_W2G107AD0301-DB-ENG-1165451.pdf

[36] PhoenixContact, "PV-CM-S 6-16." [Online]. Available: http://www.farnell.com/datasheets/1700815.pdf